ADVANCES IN ATMOSPHERIC SCIENCES, VOL. 37, AUGUST 2020, 893–911

• Original Paper •

Insights into Convective-scale Predictability in East China: Error Growth Dynamics and Associated Impact on Precipitation of Warm-Season Convective Events

Xiaoran ZHUANG[1,2], Jinzhong MIN*[1], Liu ZHANG[1], Shizhang WANG[1], Naigeng WU[1,3], and Haonan ZHU[4]

[1]*Collaborative Innovation Center on Forecast and Evaluation of Meteorological Disasters*, *Key Laboratory of Meteorological Disaster of Education*, *Nanjing University of Information Science and Technology*, *Nanjing* 210044, *China*

[2]*Jiangsu Meteorological Observatory*, *Jiangsu Meteorological Bureau*, *Nanjing* 210008, *China*

[3]*Key Laboratory of Regional Numerical Weather Prediction*, *Institute of Tropical and Marine Meteorology*, *China Meteorological Administration*, *Guangzhou* 210044, *China*

[4]*Chongqing Climate Center*, *Chongqing Meteorological Bureau*, *Chongqing* 401120, *China*

(Received 4 December 2019; revised 20 April 2020; accepted 1 June 2020)

ABSTRACT

This study investigated the regime-dependent predictability using convective-scale ensemble forecasts initialized with different initial condition perturbations in the Yangtze and Huai River basin (YHRB) of East China. The scale-dependent error growth (ensemble variability) and associated impact on precipitation forecasts (precipitation uncertainties) were quantitatively explored for 13 warm-season convective events that were categorized in terms of strong forcing and weak forcing. The forecast error growth in the strong-forcing regime shows a stepwise increase with increasing spatial scale, while the error growth shows a larger temporal variability with an afternoon peak appearing at smaller scales under weak forcing. This leads to the dissimilarity of precipitation uncertainty and shows a strong correlation between error growth and precipitation across spatial scales. The lateral boundary condition errors exert a quasi-linear increase on error growth with time at the larger scale, suggesting that the large-scale flow could govern the magnitude of error growth and associated precipitation uncertainties, especially for the strong-forcing regime. Further comparisons between scale-based initial error sensitivity experiments show evident scale interaction including upscale transfer of small-scale errors and downscale cascade of larger-scale errors. Specifically, small-scale errors are found to be more sensitive in the weak-forcing regime than those under strong forcing. Meanwhile, larger-scale initial errors are responsible for the error growth after 4 h and produce the precipitation uncertainties at the meso-β-scale. Consequently, these results can be used to explain under-dispersion issues in convective-scale ensemble forecasts and provide feedback for ensemble design over the YHRB.

Key words: convective-scale, predictability, error growth, strong forcing, weak forcing, scale interaction

Citation: Zhuang, X. R, J. Z. Min, L. Zhang, S. Z. Wang, N. G. Wu, and H. N. Zhu, 2020: Insights into convective-scale predictability in East China: Error growth dynamics and associated impact on precipitation of warm-season convective events. *Adv. Atmos. Sci.*, **37**(8), 893–911, https://doi.org/10.1007/s00376-020-9269-5.

Article Highlights:

- The warm-season convective events in the Yangtze and Huai river basin can be categorized into strong-forcing and weak-forcing regimes with respect to different forcing types.
- Error growth dynamics and the associated impact on precipitation are both regime- and scale-dependent, showing different practical predictability across convective regimes.
- The scale interaction in terms of error growth (upscale transfer and downscale cascade) is evident for both convective regimes.

1. Introduction

Warm-season extreme rainfall and associated flash floods in the Yangtze and Huai River basin (YHRB) of East China are recurring threats to lives and property (Ding, 1993; Sun and Zhang, 2012; Luo et al., 2013, 2014; Luo and Chen, 2015). The numerical weather prediction of these events remains a challenge because the forecast accuracy cannot be improved by simply increasing model resolution

* Corresponding author: Jinzhong MIN
Email: minjz@nuist.edu.cn

(Mass et al., 2002; Walser et al., 2004; Lean et al., 2008). An approach to deal with this issue is to use convective-scale ensemble forecast systems, which offers a practical way to estimate forecast uncertainties and produce probabilistic forecasts as well (Toth and Kalnay, 1997; Raynaud and Bouttier, 2016).

To understand the performance of convective-scale ensemble forecasts, it is necessary to investigate the forecast error growth (Johnson et al., 2014) of dynamic variables (horizontal wind, temperature, and water vapor mixing ratio) caused by the initial-state errors, which also helps the design of ensemble forecast systems and the explanation of warm-season convection (Melhauser and Zhang, 2012; Chen et al., 2018). For understanding the atmospheric predictability, the nature of the underlying dominant scale-interactions needs to be assessed (Bierdel et al., 2017). Studies of error growth dynamics at the convective scale have shown that moist instability and latent heat release are the predominant mechanisms for promoting rapid nonlinear error growth (Zhang et al., 2003, 2006, 2007; Tan et al., 2004; Hohenegger et al., 2006; Hohenegger and Schär, 2007), thereby explaining atmospheric predictability at the mesoscale. In convective-scale forecasts, small-scale and small-amplitude initial errors were found to grow quickly in the convective area, transfer to larger scales (upscale) and subsequently contaminate larger-scale forecasts (Tan et al., 2004; Zhang et al., 2007; Selz and Craig, 2015); this theory is summarized as the three-stage model for atmospheric error growth (Fig. 1). Sun and Zhang (2016) further highlighted butterfly effects (i.e., upscale growth of small-scale initial errors) on both intrinsic and practical limits at the meso and convective scales. On the other hand, larger-scale initial errors generally lead to greater forecast divergence of heavy-rainfall systems (Bei and Zhang, 2007) and dominate forecast accuracy (Sun and Zhang, 2016). The importance of large-scale errors is also confirmed by many other studies (Durran and Gingrich, 2014; Durran and Weyn, 2016; Weyn and Durran, 2017). Considering the presence of flow-dependent multiscale perturbations derived from ensemble data assimilation, Johnson and Wang (2016) found that the small-scale perturbations could influence precipitation forecasts after an approximate 5-h lead time. Overall, the scale interaction in terms of error growth within convective-scale forecasts requires further examination (Bierdel et al., 2017; Bachmann et al., 2019, 2020; Selz et al., 2019; Zhang, 2019).

The initial errors affect the precipitation forecast error, which in turn influences the error growth through moisture dynamics (Bei and Zhang, 2014; Klasa et al., 2019; Zhang, 2019). Nielsen and Schumacher (2016) identified the need to investigate the evolution of precipitation uncertainty due to forecast error growth. To this end, a spectral metric to assess the spatial predictability of precipitation was proposed; namely, the decorrelation scale (Surcel et al., 2015). Bachmann et al. (2019, 2020) employed the decorrelation scale to measure the predictability limit with respect to the effects of terrain and radar data assimilation. Wu et al. (2020) used the power ratio of the decorrelation scale to quantify the scale-dependent impact of initial errors on the precipitation forecast in a warm-sector heavy rainfall event. In short, the metric provides a quantitative way to establish and measure the relationship between the error growth and precipitation forecast.

The error growth of dynamic variable and precipitation forecast uncertainties measures the predictability of convective events and depends on the strengths of large-scale forcing, which is generally categorized into strong- and weak-forcing regimes (Done et al., 2006; Keil and Craig, 2011; Done et al., 2012; Flack et al., 2016; Keil et al., 2019). General results show that for events dominated by strong large-scale forcing, the large-scale initial errors play a more important role than that controlled by local instabilities (Johnson et al., 2014; Surcel et al., 2015). In a more recent study, Selz et al. (2019) highlighted the importance of identifying the up- or downscale impact of associated errors across scales on mesoscale flow for different convective regimes.

Although convective-scale predictability is believed to be highly regime-dependent, there have been few related studies on it, particularly for different convective regimes in the YHRB (Luo and Chen, 2015; Chen et al., 2018). Many studies have revealed the complexity of warm-season extreme rainfall events in this area (Zhao et al., 2007; Sun and Zhang, 2012; Zhang and Zhang, 2012; Fu et al., 2013; Luo et al., 2013; Zhang et al., 2019), and it is therefore necessary to investigate the error growth (defined as ensemble variability) dynamics and associated impact on precipitation forecasts (precipitation uncertainties) in both strong- and weak-forcing regimes for the YHRB. Furthermore, as our ultimate goal is to construct an optimal convective-scale ensemble forecast system for the YHRB region, the sensitiv-

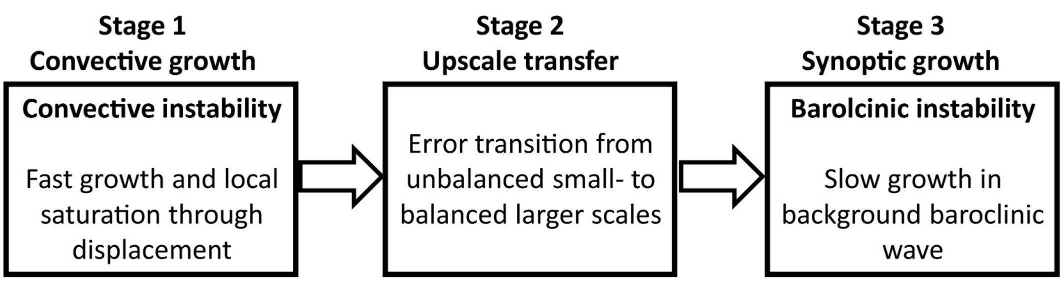

Fig. 1. Summary of the three-stage conceptual error growth model [Reprinted from (Zhang et al., 2007)].

ity of errors at different scales is also of interest (Weyn and Durran, 2019), especially for the realistic flow-dependent errors derived from an ensemble data assimilation system (Johnson and Wang, 2016; Flora et al., 2018). What is the evolution mechanism of errors at different scales within convective-scale forecasts, and how do they interact with each other to regulate the spread performance and further impact the predictability of convective weather? Although these issues are of great worth to ensemble design, few studies have focused on them.

To deal with the above concerns, we design several ensembles of convective-scale simulations using an Observation System Simulation Experiment (OSSE) setup to investigate the regime-dependent error growth for 13 warm-season convective events. The objectives of this study are: (1) to explore the error growth characteristics within 12-h forecast range in both strong- and weak-forcing regimes over the YHRB and identify possible differences between the two subsets; (2) to understand the impact of error growth on precipitation forecasts across spatial scales; and (3) to investigate the sensitivity of lateral boundary and realistic flow-dependent initial condition (IC) errors at different scales. The results of this investigation provide insights into understanding the impacts of realistic flow-dependent perturbations implemented in convective-scale ensemble forecasts, particularly those related to under-dispersion issues in current convective-scale ensemble forecasts (Tennant, 2015; Sun and Zhang, 2016), and offer further suggestions for the improvement of an optimal convective-scale ensemble forecast for the YHRB.

The rest of this paper is organized as follows: The model and ensemble design approaches are described in section 2, along with details of analysis methods and the cases examined. Results from synthetic analysis and typical case studies are presented in sections 3 and 4. Section 5 provides a summary and discussion.

2. Methods and experiments

2.1. *Model configuration*

The Advanced Research core of the Weather Research and Forecasting (WRF) model, version 3.7.1 (Skamarock et al., 2008), is utilized as the numerical model. A one-way nested framework is designed with 180 × 180 and 258 × 258 horizontal grid points for 18- and 3-km grid spacing, respectively (Fig. 2). There are 41 terrain-following hydrostatic-pressure vertical levels and a model top of 10 hPa in both outer and inner domains.

The ICs and lateral boundary conditions (LBCs) are derived from the U.S. National Centers for Environmental Prediction Global Forecast System (GFS) operational analysis data. The physical parameterization schemes include the WSM6 microphysics scheme (Hong and Lim, 2006), Yonsei University boundary layer scheme (Hong et al., 2006), RRTM longwave radiation scheme (Mlawer et al., 1997), and Goddard shortwave radiation scheme (Chou and Suarez, 1999). Additionally, the Grell-3 cumulus scheme (Grell and Dévényi, 2002) is used in the inner domain.

2.2. *OSSE framework and ensemble generation*

Following Zhuang et al. (2020), an ensemble data assimilation and forecast system (Wang et al., 2013) is constructed (Fig. 3) to generate flow-dependent IC and LBC perturbations. The Ensemble Square Root Filter approach proposed by Whitaker and Hamill (2002) is employed as the data assimilation method. For the present study, the system is modified to run in an OSSE setup to remove model uncertainties (Yussouf and Stensrud, 2012; Gasperoni et al., 2013; Johnson and Wang, 2016; Madaus and Hakim, 2017).

To create a "true" atmospheric state, we first perform a 36-h nature run initialized from the GFS analysis 24 h before the analysis time for each case with a 3-km resolution covering the outer domain (Fig. 2a). The mesoscale

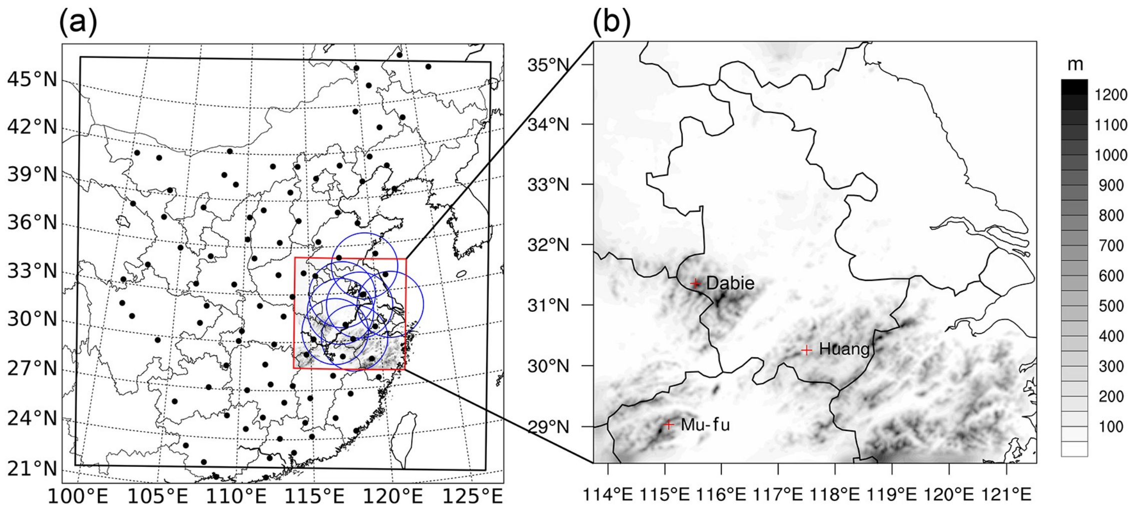

Fig. 2. (a) Model domain configuration: the black square indicates the outer domain (18-km resolution); the red square indicates the inner domain (3-km resolution); black dots show the distribution of simulated sounding datasets; blue circles show locations of the seven radar sites. (b) Terrain height within the inner domain, the Dabie Mountains (31°N, 116°E), Huang Mountains (30°N, 117.5°E), and Mu-fu Mountains (29°N, 115°E).

sounding datasets are then generated at randomly chosen locations within China's mainland (Fig. 2a) and interpolated from the "true" run with observation errors of 2.5 m s^{-1}, 1.2 K, and 0.005 kg kg^{-1} for wind velocity, temperature, and water vapor, respectively (Snook et al., 2015). For the inner domain, the "true" run is interpolated to seven real CINRAD-SA radars (Zhu and Zhu, 2004) (Fig. 2b) with observation errors of 2 m s^{-1} and 5 dBZ for radial velocity and reflectivity (Johnson et al., 2015).

We then generate the initial ensemble in the outer domain, by adding analysis perturbations from the first 30-member European Centre for Medium-Range Weather Forecasts global ensemble prediction products (Hagedorn et al., 2008; Hagedorn et al., 2012) to temperature, horizontal wind, and water vapor mixing ratio in the ICs and LBCs. After that, the mesoscale sounding data assimilation for the outer domain is initialized at 0000 or 1200 UTC (0008 or 2000 LST) for each case (Table 1) over a 24-h period with 3-h intervals. For the inner domain, the initial ensemble is obtained by downscaling the analysis states at the seventh assimilation cycle in the outer domain using the WRF "ndown" tool (Daniels et al., 2016). The radar data (including reflectivity and radial velocity) are then assimilated for 3-h with 10-min intervals in the inner domain, while the outer domain provides larger-scale LBC perturbations every 15-min during the assimilation cycles.

Table 1. Summary of cases.

Number	Start time	Subset
1	0000 UTC 23 June 2013	Weak forcing
2	0000 UTC 5 July 2013	Weak forcing
3	1200 UTC 6 July 2013	Strong forcing
4	0000 UTC 7 July 2013	Weak forcing
5	0000 UTC 21 July 2013	Weak forcing
6	0000 UTC 22 July 2013	Weak forcing
7	0000 UTC 1 June 2014	Strong forcing
8	0000 UTC 15 June 2014	Strong forcing
9	0000 UTC 25 June 2014	Strong forcing
10	0000 UTC 26 June 2014	Weak forcing
11	1200 UTC 1 July 2014	Strong forcing
12	0000 UTC 12 July 2014	Weak forcing
13	1200 UTC 24 July 2014	Strong forcing

The horizontal and vertical covariance localization radii for the outer domain are 120 km and 6 km, and the corresponding values in the inner domain are 20 and 5 km (Wang et al., 2013; Snook et al., 2015), respectively. To maintain spread within the assimilation cycles, a multiplicative covariance inflation of 1.15 (Anderson and Anderson, 1999; Tong and Xue, 2005) and a relaxation inflation of 0.5 to prior ensemble variability (Zhang et al., 2004) are applied to the outer and inner domains.

The control experiment (CTRL) uses the first 20 members of the ensemble analysis in the inner domain and the LBC perturbations are provided by the outer domain ensemble forecasts and perform 12-h convective-scale ensemble forecasts (Fig. 3). Several sensitivity experiments (IC_MULTI, IC_SMALL, IC_TRANS, and IC_LARGE) are conducted to further clarify the scale-based sensitivity of errors. These experiments employ the same LBCs from the ensemble mean analysis of the outer domain (no LBC perturbations) and differ in initial perturbations that are constructed in three steps: (i) subtract the ensemble mean from each analysis state to obtain intermediate perturbations; (ii) scale each perturbed variable by retaining information at determined spatial scales; and (iii) add the scaled perturbations back to the ensemble mean (Table 2). Specifically, IC_MULTI uses the same IC perturbations as CTRL with LBC perturbations excluded to investigate the sensitivity of larger-scale LBC errors. By retaining the small-scale components of the flow-dependent IC perturbations, the up-amplitude and upscale processes of small-scale initial errors and the associated impact on precipitation can be isolated and examined via IC_SMALL. By retaining the larger-scale components of the IC perturbations, the evolution and the associated impact of larger-scale initial errors on precipitation can be isolated and examined via IC_LARGE. The definition of scale range is specified in section 2.3.

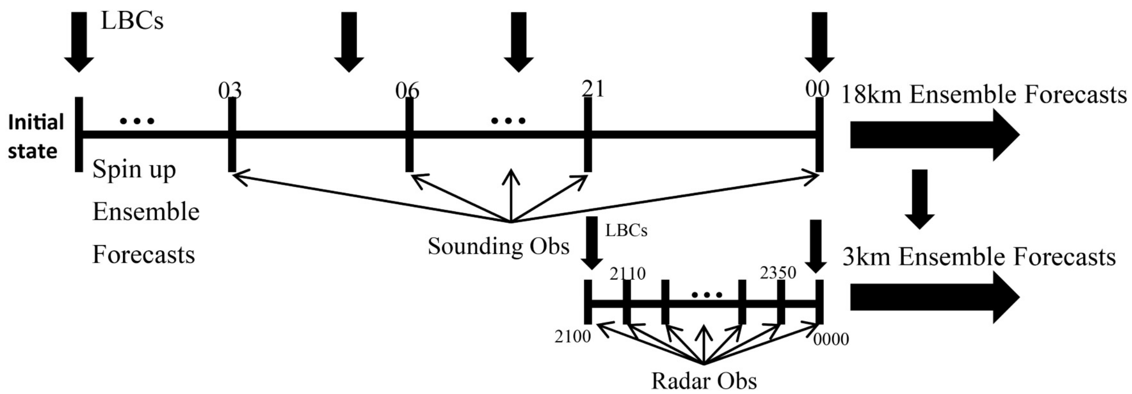

Fig. 3. Schematic of the ensemble data assimilation configuration. The outer-domain ensemble data assimilation is initialized at 0000 or 1200 UTC for each case, while the inner domain ensemble data assimilation is initialized 21 h after the outer domain initialization using the outer-nest ensemble for both the initial and boundary conditions. "Obs" indicates observations.

Table 2. Summary of IC perturbations and LBC perturbations used in the ensemble experiments.

Experiment	IC perturbations	LBC perturbations
CTRL	Flow-dependent_3 km	Flow-dependent_18 km
IC_MULTI	Flow-dependent_3 km	None
IC_SMALL	Filtered information < 36 km from Flow-dependent_3 km	None
IC_TRANS	Filtered in formation > 36 km and < 120 km from Flow-dependent_3 km	None
IC_LARGE	Filtered information > 120 km from Flow-dependent_3 km	None

2.3. *Representation of scale-dependent error growth*

The forecast error is quantified using the difference total energy (DTE; Zhang et al., 2007):

$$\mathrm{DTE}(\lambda)_{i,j,k,t,m} = \frac{1}{2}\left[u(\lambda)'^{2}_{i,j,k,t,m} + v(\lambda)'^{2}_{i,j,k,t,m} + \frac{C_p}{T_r} t(\lambda)'^{2}_{i,j,k,t,m}\right], \quad (1)$$

where u',v', and t' are the differences of zonal wind, meridional wind, and temperature from the ensemble mean, respectively ($C_p = 1004.9\ \mathrm{J\ kg^{-1} K^{-1}}$ and $T_r = 270$ K). The subscripts i, j, k, t, m, and λ represent the x-direction, y-direction, vertical level, forecast time, ensemble member, and the spatial scale.

To measure the scale-dependent error growth, we classify the spatial scale into three scale ranges (Zhuang et al., 2020): small scale (36 km $\geqslant$ wavelength); transition scale (120 km $\geqslant$ wavelength > 36 km); and larger scale (wavelength > 120 km). To obtain variable fields at different scales, the discrete cosine transform (DCT) (Denis et al., 2002; Surcel et al., 2015; Wu et al., 2020) method is used. Compared to traditional Fourier transform methods, DCT is able to avoid discontinuity problems at domain boundaries.

We also introduce a vertical function (Nielsen and Schumacher, 2016) to calculate the two-dimensional root-mean vertically integrated DTE (RMDTE). To compare the error growth between different convective regimes, the normalized root-mean vertically integrated DTE (NRMDTE) (Nielsen and Schumacher, 2016; Klasa et al., 2019) at different scales is calculated to eliminate the variability independent of the magnitude of the total background flow (Appendix A).

2.4. *Representation of spatial precipitation uncertainty*

To evaluate spatial precipitation uncertainties, the decorrelation scale method proposed by Surcel et al. (2015) is applied. As described in that study, complete decorrelation of ensemble forecasts can be considered as a lack of precipitation predictability by the ensemble at a given scale λ_0. For the scale $\lambda \leqslant \lambda_0$, there is no precipitation predictability. For the scale $\lambda \geqslant \lambda_0$, the precipitation fields of ensemble members are correlated, indicative of some predictability. The power ratio is used to quantitatively assess the precipitation uncertainty (Wu et al., 2020):

$$R(\lambda) = \frac{\sum_{m=1}^{n} \mathrm{Var}(p_m(\lambda))}{\mathrm{Var}\left(\sum_{m=1}^{n} p_m(\lambda)\right)}, \quad (2)$$

where $\mathrm{Var}(p_m(\lambda))$ is the variance of the precipitation field $p_m (m = 1, \ldots, n)$ at spatial scale λ. The value of $R(\lambda)$ varies from 1 / n to 1, with a larger value corresponding to higher uncertainty and lower precipitation predictability. In general, a threshold value of $R(\lambda) = 1$ means the complete loss of predictability at scale λ, while in this study, the threshold is set to 0.9 to eliminate noise without introducing any significant bias (Judt, 2018; Wu et al., 2020). Quantitative investigations of precipitation uncertainty are then conducted by comparing $R(\lambda)$ for different ensemble designs at different forecast lead times.

2.5. *Case selection*

Thirteen mei-yu-season heavy-rainfall events (June and July 2013–2014) (Liu et al., 2012; Sun and Zhang, 2012; Luo and Chen, 2015) over the YHRB are selected, ranging from local self-organized convective events to synoptically driven mei-yu-front events. Based on the convective adjustment timescale τ_c (Appendix B) calculated with the deterministic forecast in the inner domain (initialized with the ensemble mean analysis), all 13 cases are quantitatively classified into two categories based on the convective adjustment timescale. The typical 6-h (Zimmer et al., 2011; Keil et al., 2014) threshold is used to distinguish strong-forcing events from weak-forcing events (Table 1).

Figure 4a shows the evolution of τ_c with corresponding convective available potential energy (CAPE; Fig. 4b) for cases in each subset. Note that τ_c for the weak-forcing subset is markedly higher than that of the strong-forcing subset with a more remarkable semidiurnal cycle of CAPE. Figures 5c and d show the frequency of 1-h precipitation exceeding 0.5 mm h^{-1} in both strong- and weak-forcing regimes for the true state. The strong-forcing events exhibit a southwest–northeast frequency belt along the mei-yu front (Fig. 5c), which is consistent with the frontal rainfall events (Sun and Zhang, 2012). The weak-forcing events exhibit a scattered pattern near the Dabie Mountains, Huang Mountains, and Mu-fu Mountains (Chen et al., 2016), with frequency maxima 1°–3° to the south of the northeast–southwest-oriented weak mei-yu front (Fig. 5d). The wind fields also differ between strong- and weak-forcing regimes, with the strong-forcing cases having stronger wind speed (Fig. 4c) and cyclonic shear (Fig. 5a) while the weak-forcing cases are generally characterized by weaker large-scale advection (Fig. 4d and Fig. 5b) in which the CAPE is higher (Figs. 4a). These environmental features are in accordance with Klasa et al. (2019), as they also found stronger large-scale advection and lower CAPE for strong-forcing events,

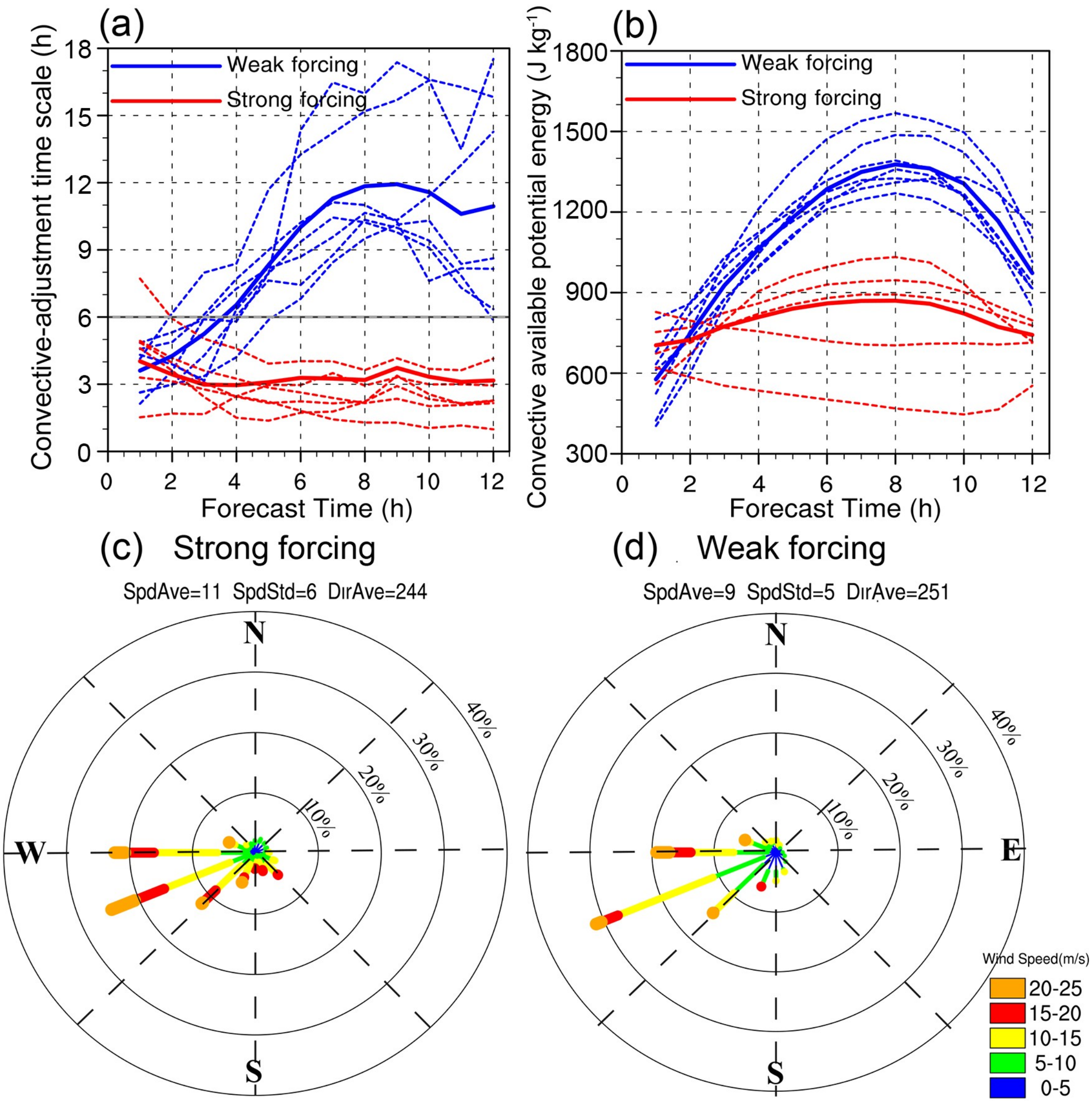

Fig. 4. The (a) convective-adjustment time scale τ_c (units: h) and (b) CAPE (units: J kg^{-1}) averaged over areas with rainfall higher than 0.5 mm h^{-1}. The black line in (a) is the 6 h threshold for regime classification. The dashed lines indicate each case while the thick solid lines represent average value for each subset. (c, d) Wind rose variation between 1000 and 100 hPa for (c) strong-forcing and (d) weak-forcing cases. The concentric rings show the frequency of wind direction and the colors indicate the magnitude of wind speed.

supporting our application of τ_c.

3. Regime-dependent error growth and associated impact on precipitation

In this section, error growth across convective regimes and its associated impact on precipitation are examined by assessing the NRMDTE of CTRL and the corresponding evolution of precipitation uncertainties (R) for the strong- and weak-forcing regimes.

3.1. *Spatiotemporal characteristics of total error growth*

Figure 6 shows the temporal evolution of total NRMDTEs for both strong-forcing (Fig. 6a) and weak-forcing (Fig. 6e) regimes. In the strong-forcing regime, the mean total NRMDTE manifests a moderate evolution, while in the weak-forcing regime it shows a larger variation with a maximum in the afternoon (4–8 h), the variation of which is in accordance with the daytime phase diurnal peak of convection in the YHRB (Sun and Zhang, 2012).

Figures 7 and 8 give the total NRMDTEs and ensemble mean precipitation (time–longitude and time–latitude diagrams) averaged over cases in each subset. The events under strong forcing exhibit a strong easterly progression (Fig. 7a, Fig. 8a), while a relatively stationary feature for both variables appears in the weak-forcing regime (Fig. 7e and Fig. 8e). These results indicate that forecast errors can be transported to a broad area covered by the influence of a strong frontal system during the strong-forcing regime, but the errors are often restricted to a smaller area in the weak-for-

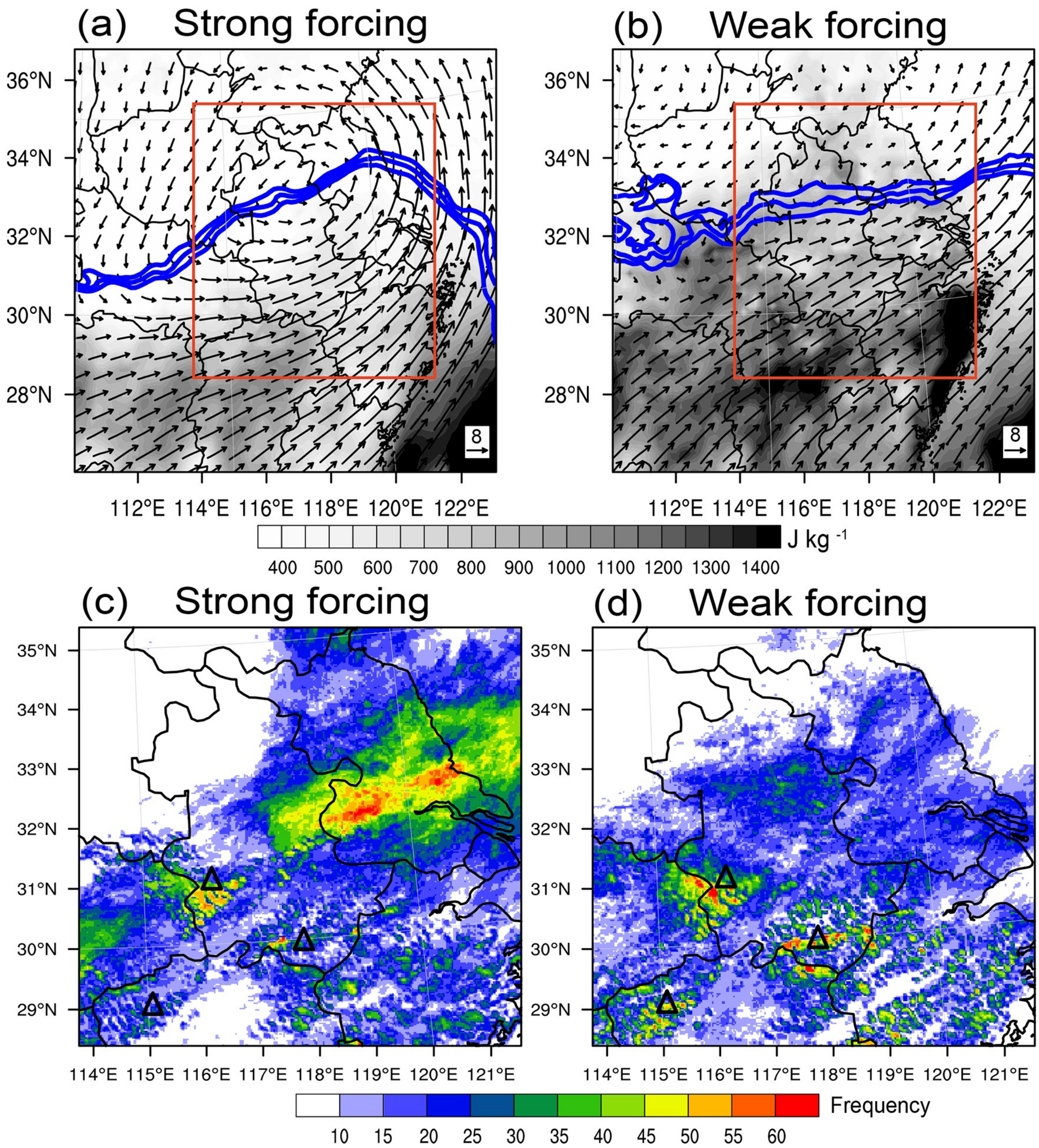

Fig. 5. (a, b) Ensemble-mean 850-hPa wind vector (units: m s^{-1}) and equivalent potential temperature (blue solid contours lines, 344–348 K, 2 K interval, indicating the location of the mei-yu front) averaged over cases for the (a) strong- and (b) weak-forcing regime calculated from the outer domain ensemble. The red boxes indicate the inner domain. (c, d) Precipitation frequency computed from the observed hourly precipitation exceeding 0.5 mm h^{-1} for the (c) strong- and (d) weak-forcing regime. The black triangles indicate the mountains shown in Fig. 2.

cing regime. In addition, the NRMDTE (Fig. 8e) increases with forecast lead time toward lower latitudes in the weak-forcing regime. It is speculated that this southward motion is associated with the small-scale convection (e.g., isolated storms, squall lines, or multicell storms) triggered by local factors in the southern region. Overall, these results indicate that forecast errors often closely follow the precipitation system.

3.2. *Spatiotemporal characteristics of error growth at different scales*

We further analyze error growth at and across spatial scales. In general, the trends of NRMDTEs for different cases are generally consistent with each other for each subset (gray lines in Fig. 6), confirming our classification of cases. Similar to Zhang et al. (2007), we conclude the scale-dependent error growth into three stages for the strong- and weak-forcing subsets, respectively. In the strong-forcing regime, a “stepwise” increase with increasing spatial scale that is similar to the three-stage conceptual model proposed in Zhang et al. (2007) is observed. Stage 1 corresponds to rapid up-amplitude growth and saturation that is defined as the point at which the NRMDTE reaches its maximum value (Zhang, 2019) of small-scale errors around the first 2 h

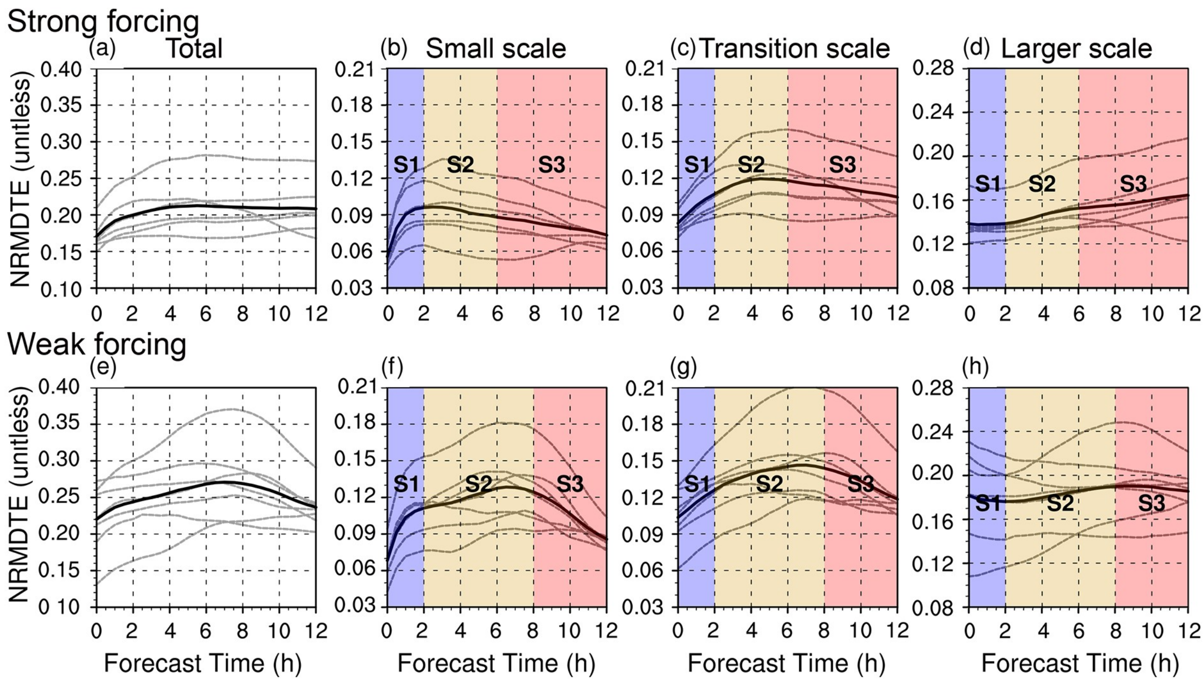

Fig. 6. Time series of the 12-h NRMDTE of CTRL at different scales for (a–d) strong- and (e–h) weak-forcing cases: (a, e) total NRMDTE; (b, f) small-scale NRMDTE; (c, g) transition-scale NRMDTE; (d, h) large-scale NRMDTE. The thick black curves represent the NRMDTEs averaged over cases of each subset while the dashed gray curves represent the NRMDTEs for each case. S1–S3 indicates the error growth stages for each subset.

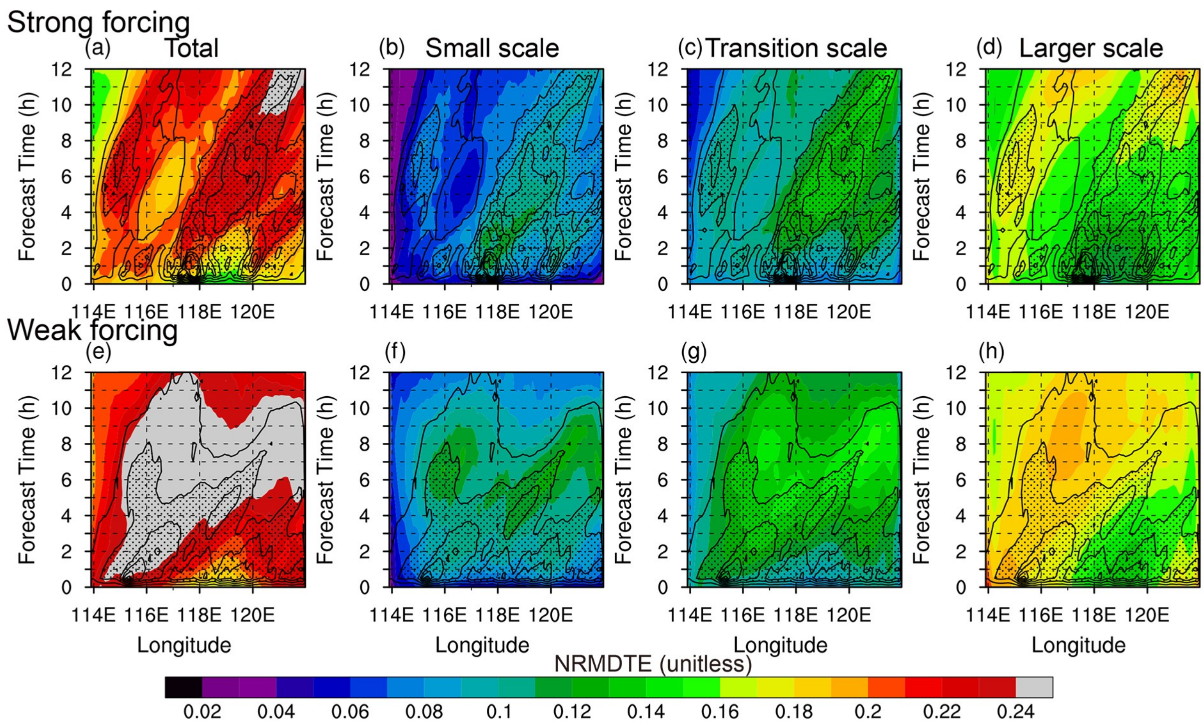

Fig. 7. Hovmöller (meridionally averaged mean NRMDTE at different scales, time–longitude) diagrams for the NRMDTE of CTRL averaged over cases for the (a–d) strong- and (e–h) weak-forcing regime: (a, e) total NRMDTE; (b, f) small-scale NRMDTE; (c, g) transition-scale NRMDTE; (d, h) larger-scale NRMDTE. Black contours (0.2–1.6 mm, contoured every 0.2 mm) indicate the ensemble mean 0.5 h accumulated precipitation and the shading denotes regions with precipitation exceeding 0.6 mm.

(Figs. 6b, 7b and 8b). This result indicates the rapid predictability loss at the relevant scales (Lorenz, 1969; Judt, 2018).

At Stage 2, transition-scale NRMDTE remains increasing and slightly spread beyond the convective zones (Figs. 7c

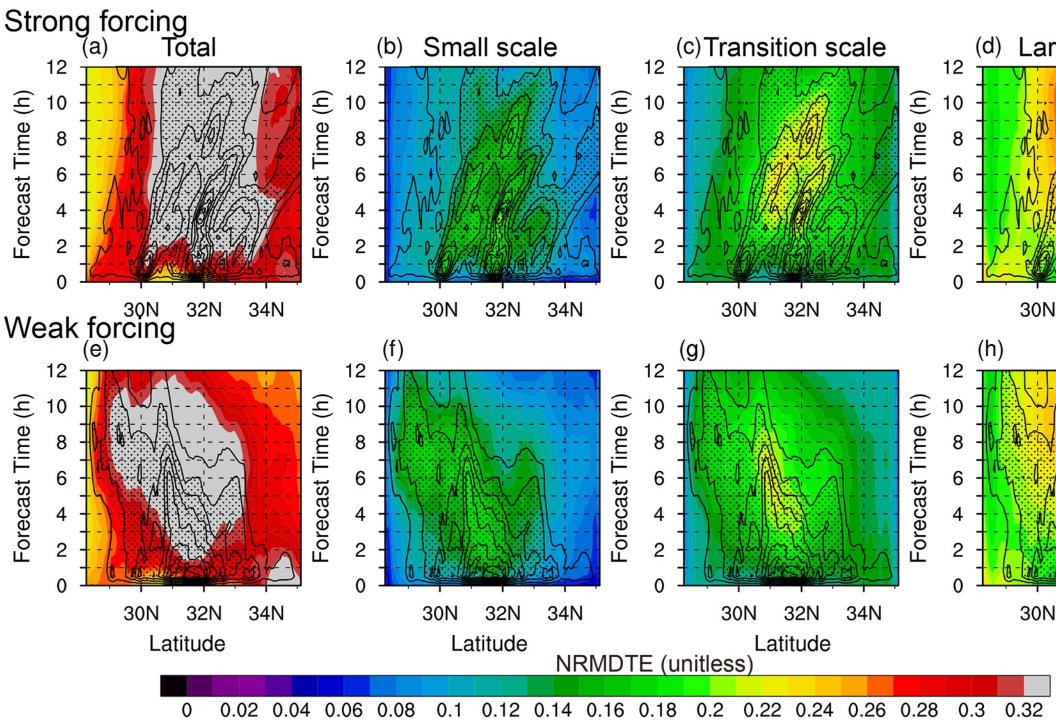

Fig. 8. As in Fig. 7 but for zonally averaged NRMDTE averaged over cases in each subset.

and 8c), which is attributable to an upscale transfer of small-scale errors. During Stage 3, transition-scale NRMDTE saturates at around 6 h while larger-scale NRMDTE remains a slight increase (Figs. 6d, 7d and 8d), which may gradually influence mesoscale predictability from the initial higher-latitude areas where the mei-yu front formed, demonstrating an interaction between the convective and larger scales (Nielsen and Schumacher, 2016).

In the weak-forcing regime, small-scale errors (Figs. 6f, 7f and 8f) experience a rapid up-amplitude growth similar to that under strong forcing during the first 2 h (Stage 1) but remain a steeper and longer increase during 2–8 h (Stage 2), demonstrating lower predictability than that under strong forcing (Keil et al., 2014; Zhuang et al., 2019). Transition-scale errors (Figs. 6g, 7g and 8g) experience an evolution similar to but slightly smoother than that of small-scale errors during the same period. Such evolutions of the NRMDTEs for the small and transition scales are likely driven by the convection diurnal peak, in which convective events usually strengthen during the afternoon due to solar heating. After 8 h (Stage 3), small- and transition-scale NRMDTEs both exhibit reduction, albeit with a slight increase in larger-scale NRMDTE (Figs. 6h, 7h and 8h), reflecting the relationship between the moist convection and error growth is weaker at the larger scale.

Overall, the above findings confirm that upscale error growth (Zhang et al., 2007; Selz and Craig, 2015) is evident over the YHRB, but more obvious for the strong-forcing regime. Meanwhile, for the weak-forcing regime, the error growth is largely modulated by the convection afternoon peak (Nielsen and Schumacher, 2016; Klasa et al., 2019; Wu et al., 2020). This result highlights a strong regime-dependent feature. In addition, we also find the peak of forecast errors in the weak-forcing regime is most prominent for the small and transition scales. As the diurnal cycle of convection can be regarded as "external forcing" from a quasi-stationary terrain or solar forcing, the peak (or other big fluctuations) of error growth for the weak-forcing regime should be regarded as added value superimposed on the basic error growth emerging from the strong moist convection (Nielsen and Schumacher, 2016) and explain the scale-dependent error growth.

Note that larger-scale NRMDTEs are slightly damped during the first few hours in both regimes (Figs. 6d and h). This may be due to the poor representation of synoptic- and subsynoptic-scale information using small-domain convective-scale ensemble forecasts. A similar phenomenon can also be found in previous studies (Bei and Zhang, 2007; Zhang, 2019). A comparison of the NRMDTEs with those from a larger-domain experiment (not shown) reveals that the relatively small domains and the terrain along the southern boundary do not influence the 12-h evolution trend of forecast error. However, the terrain at the boundary does have a slight negative impact on the up-amplitude error growth at the small-scale, particularly for the terrain-forcing events under weak forcing, which requires further evaluation beyond the scope of this study.

3.3. *Impact of error growth on precipitation*

A novelty of this study is a systematic examination of the impact of error growth on the precipitation forecast. Previous studies have revealed a strong correlation between error growth and precipitation (Johnson et al., 2014; Flack et al., 2018), but they did not consider this issue in terms of spa-

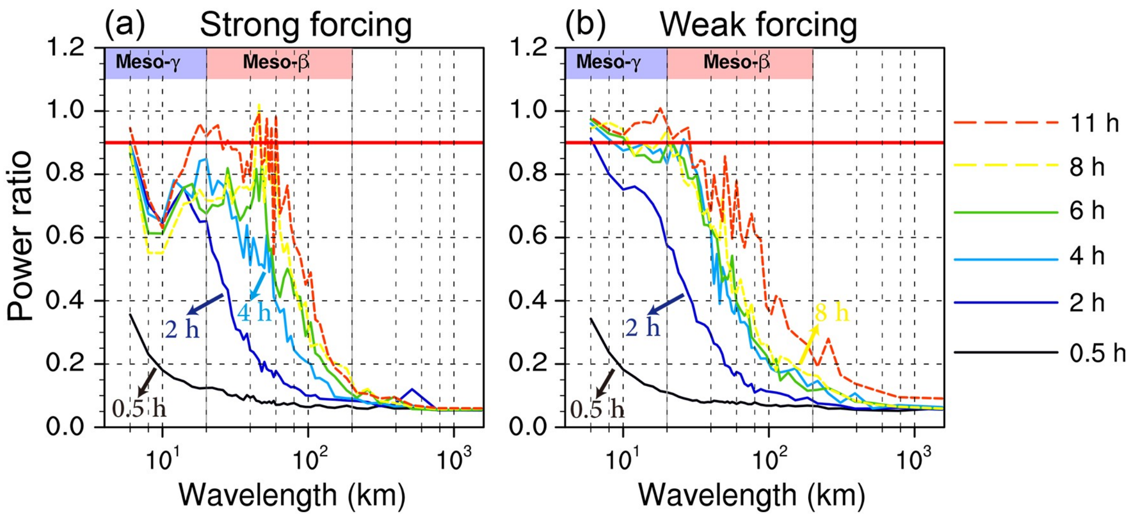

Fig. 9. Temporal evolution of the power ratio (R) for 0.5 h accumulated precipitation calculated from CTRL averaged over cases for the (a) strong- and (b) weak-forcing regime. The red reference line represents total loss of precipitation predictability. The dashed lines correspond to Stage 3 of error growth.

tial scales.

Figure 9 shows the power ratio [Eq. (2), hereafter referred to as R for brevity] averaged over cases within each subset at different lead times, which is used to quantitatively assess the precipitation uncertainty. In Stage 1 (0.5 h, black curves) for both strong- and weak-forcing regimes, the rapid increase of the flow-dependent small-scale errors (Figs. 6b and f) leads to increased R originated from small scales. The distribution of R decreases monotonically with increasing scale, revealing an approximately positive relationship between error growth and precipitation uncertainties in the small scale.

A divergence occurs between the strong- and weak-forcing regimes at the start of Stage 2 (2 h, blue curves). For the strong-forcing regime, R features fluctuations on scales around 20 km, with the distribution peak shifting to the larger scales until approximately 6 h (the end of Stage 2), implying a loss of predictability at around 60 km (Fig. 9a). This indicates the impact of upscale error growth on precipitation at the meso-β-scale (Fig. 9a) and can be explained by the rapid displacement of individual cells driven by large-scale forced ascent (Done et al., 2006; Zhang et al., 2007; Liu and Tan, 2009; Flack et al., 2018) around the mei-yu front. After 6 h (Stage 3), when the NRMDTEs generally reach saturations at both the small and transition scales (Figs. 6b and c), R continues to increase as a result of the up-amplitude growth of larger-scale errors (Fig. 6d) with the distribution peak remaining unchanged.

For the weak-forcing regime, with the consistent, up-amplitude growth of small- and transition-scale NRMDTEs (Figs. 6f and g) at Stage 2 (2–8 h), R retains a monotonic distribution with the peak centered at the grid scales (Fig. 9b), implying a thorough predictability loss at the meso-γ-scale as a result of the localized error growth (Fig. 7e). After 8 h, the small- and transition-scale NRMDTEs become saturated (Figs. 6f and g) and R displays increase at all scales, particularly at the larger scales, corresponding to the subsequent upscale error growth.

Overall, these results demonstrate a strong correlation between error growth and precipitation in a scale-dependent manner. Specifically, the up-amplitude error growth increases the magnitude of precipitation uncertainty while the upscale error transfer before saturation at a given scale influences its spatial distribution. These results also demonstrate how multiscale initial perturbations impact precipitation at different scales, particularly under various large-scale forcings.

4. Sensitivity of regime-dependent error growth to the lateral boundary and IC errors at different scales

To further investigate the differences of predictability across convective regimes, the sensitivity of the lateral boundary and flow-dependent initial errors at different scales is assessed in this section. Although previous studies focusing on the amplitude of error reached significant conclusions with respect to predictability at the convective scale (Nielsen and Schumacher, 2016; Zhang et al., 2016; Flora et al., 2018), there have been relatively few studies on the sensitivity of realistic flow-dependent errors at different scales that are directly relevant to convective- and large-scale forcing or related to the formulation of data assimilation strategies.

4.1. *Role of larger-scale lateral boundary errors*

In convective-scale ensemble forecasts, LBC perturbations generally exert larger-scale errors to the inner domain from LBCs in a one-way nested configuration (Nutter et al., 2004) and dominate the ensemble variability after the first 6–12 h (Vié et al., 2011; Kühnlein et al., 2014). Figure 10 shows a comparison of CTRL (black curves) and IC_MULTI (gray curves), which reveals that the LBC errors exert impacts on the error growth at the transition and larger scales for both subsets. Such impacts can also be seen from the comparison between CTRL and IC_MULTI in terms of a spatial view as shown in Fig. 8 and Fig. 11. In addition, the relative difference of total NRMDTE between IC_MULTI and CTRL shows a quasi-linear increase with time and reaches 30% at 12 h, reflecting the results from

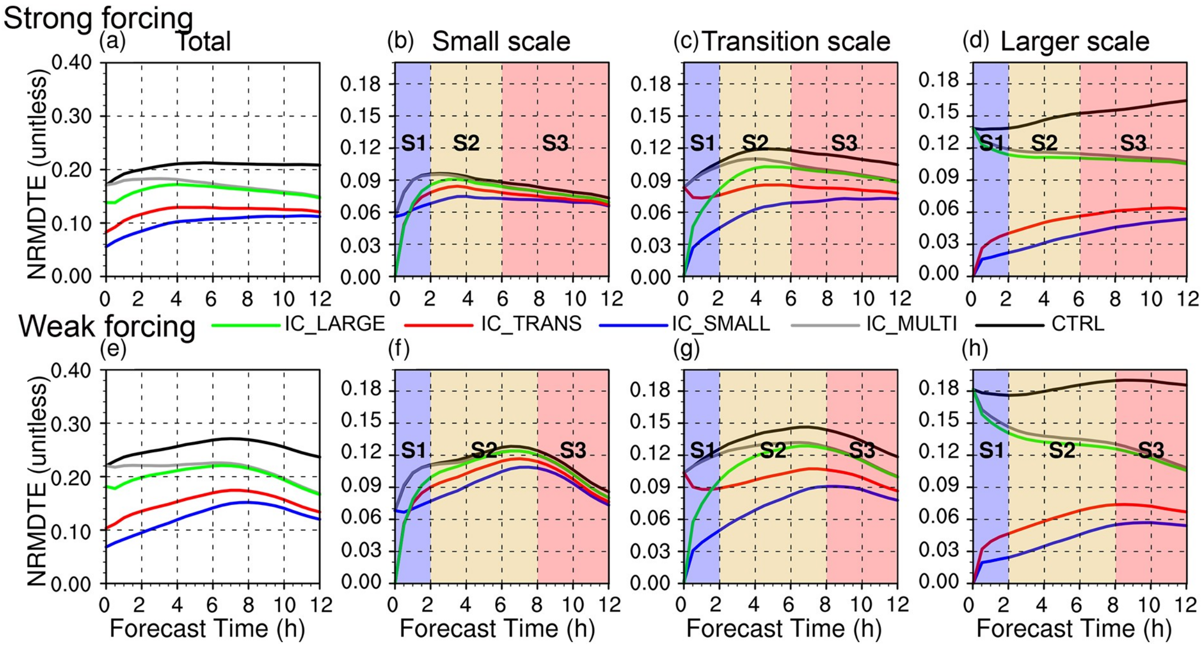

Fig. 10. Time series of 12-h mean NRMDTE at different scales of CTRL (black curves), IC_MULTI (gray curves), IC_SMALL (blue curves), IC_TRANS (red curves), and IC_LARGE (yellow curves) averaged over cases for the (a–d) strong- and (e–h) weak-forcing regime: (a, e) total NRMDTE; (b, f) small-scale NRMDTE; (c, g) transition-scale NRMDTE; (d, h) larger-scale NRMDTE. S1–S3 indicate the error growth stages for each subset.

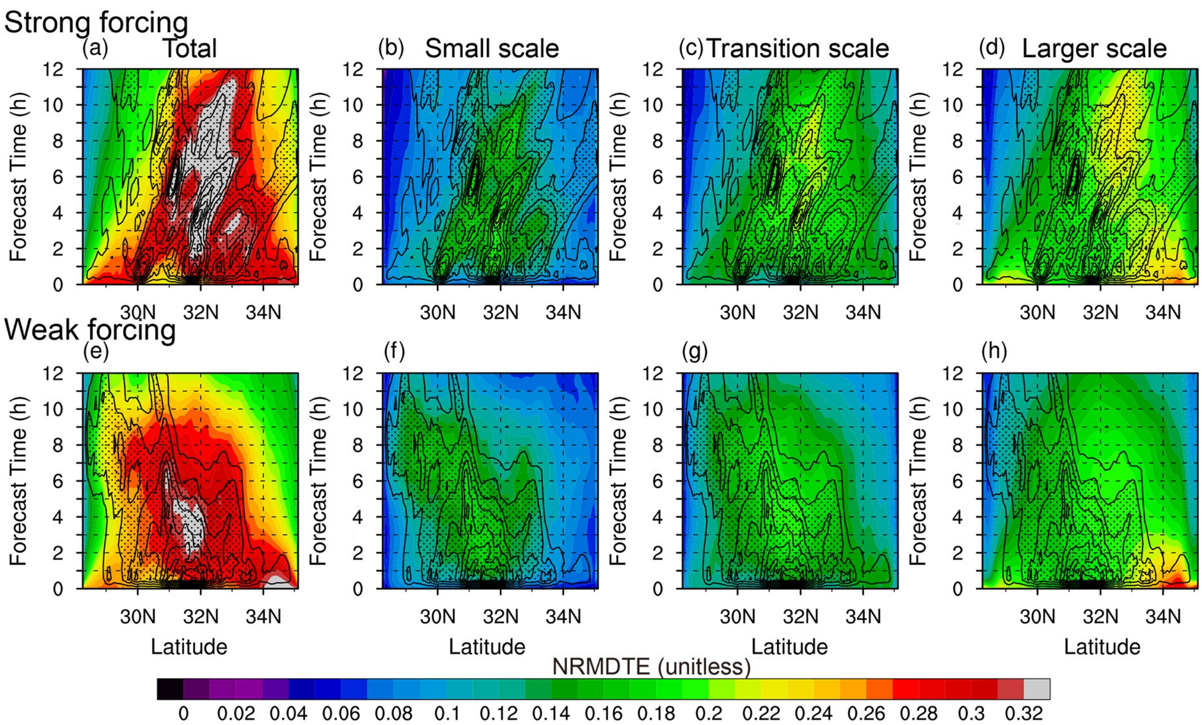

Fig. 11. Zonally averaged Hovmöller (time–latitude) diagrams for the NRMDTE of IC_MULTI averaged over cases for the (a–d) strong-forcing and (e–h) weak-forcing regime: (a, e) total NRMDTE; (b, f) small-scale NRMDTE; (c, g) transition-scale NRMDTE; (d, h) larger-scale NRMDTE. Black contours (0.2–1.6 mm, contoured every 0.2 mm) indicate the corresponding ensemble mean 0.5 h accumulated precipitation and the shading denotes regions with precipitation exceeding 0.6 mm.

Zhang (2019), which is primarily attributable to the larger-scale component (Figs.10d, h and Fig. 11d, h).

Regarding the impact of LBC errors on precipitation uncertainty, we find a clear decay of R during the strong-forcing regime (Fig. 12a) after 4 h. This finding demonstrates a practical predictability limit from LBC errors, as R decays in both amplitude and spatial scale of the distribution peak in IC_MULTI after 4 h, revealing under-dispersion issues compared with CTRL and the need to improve LBC perturbations for convective-scale ensemble forecasts. This feature can also be identified from 4–6 h in Fig. 10c, as the transition-scale NRMDTEs for IC_TRANS, IC_LARGE, and IC_MULTI all experience decays, while larger-scale NRMDTEs cease increasing afterward (Fig. 10d). Accordingly, this time period can also be regarded as a bifurcation point at which transition-scale errors can either reach a theoretical limit or continue to grow upscale to larger scale and impact precipitation at the meso-β-scale. Comparably, though R in IC_MULTI also exhibits a decay relative to CTRL under the weak-forcing regime (Fig. 12b), it nevertheless continues to increase with time. In short, these results support the hypothesis that error growth and its associated impact on precipitation can be constrained by the large-scale control imposed by the LBCs (Nielsen and Schumacher, 2016; Klasa et al., 2019), particularly for the strong-forcing regime.

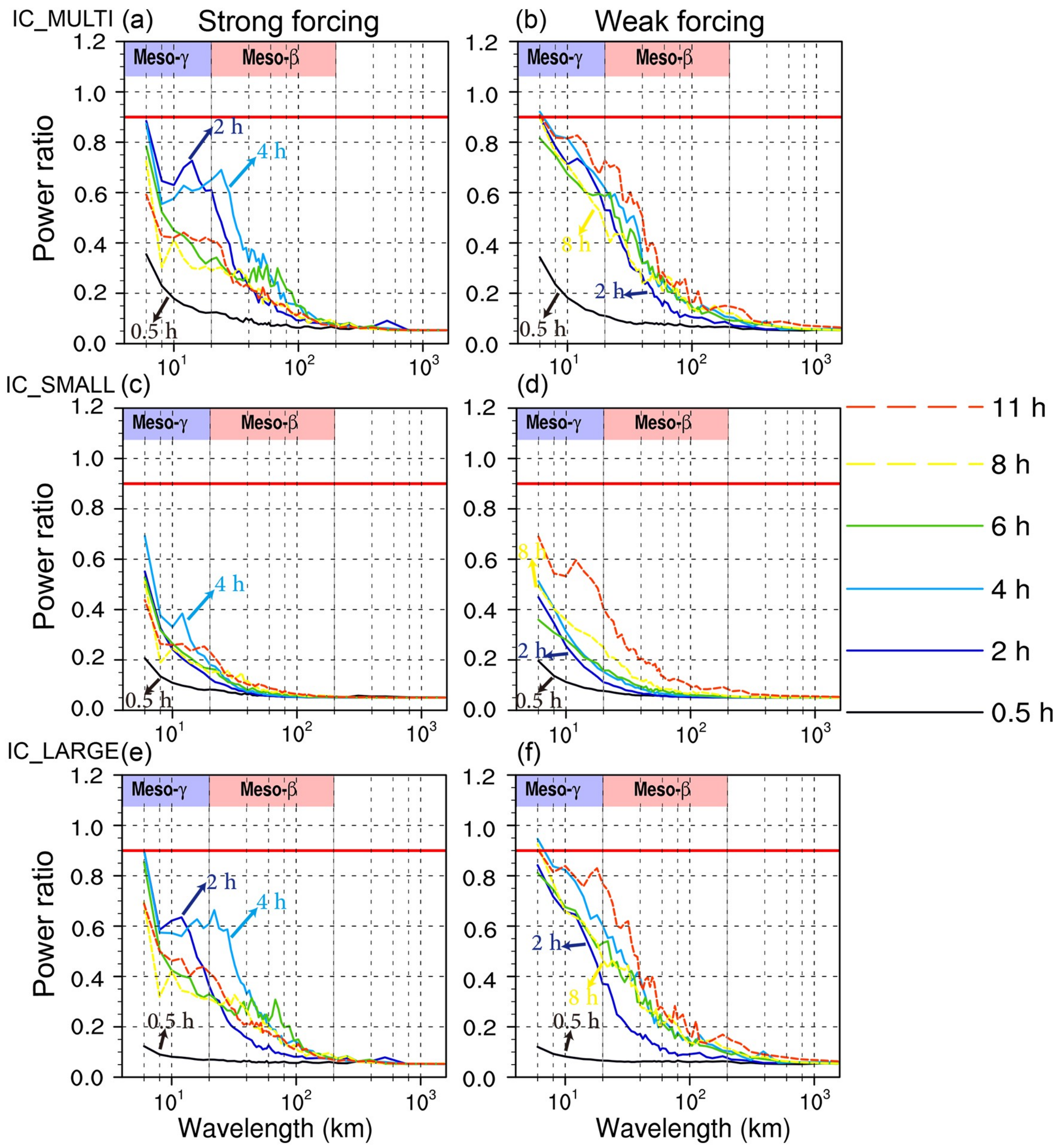

Fig. 12. Temporal evolution of the power ratio (R) for 0.5 h accumulated precipitation of (a, b) IC_MULTI, (c, d) IC_SMALL and (e, f) IC_LARGE averaged over cases for the (a, c, e) strong- and (b, d, f) weak-forcing regime. The red reference line represents total loss of precipitation predictability. The dashed lines indicate Stage 3 when larger-scale errors become dominant.

4.2. *Role of small-scale initial errors*

Small-scale initial errors can grow up-amplitude and upscale predominated by moist convection (Hohenegger et al., 2006; Zhang et al., 2007; Selz and Craig, 2015). Figure 13 shows that the large NRMDTE values at the transition scale (Figs. 13c and g) and larger scale (Figs. 13d and h) appear later than those of the small scale (Figs. 13b and f) for IC_SMALL, indicative of the upscale transfer. In addition, the total NRMDTE of IC_SMALL (blue curves in Figs. 10a and e) is substantially lower than that of IC_MULTI (gray curves in Figs. 10a and e), with reduced magnitude of mean small-scale NRMDTE at Stage 1 (Figs. 10b and f) and subsequent stages through a weaker upscale transfer. However, for both convective regimes, we find the evolution trend [i.e., the stepwise feature under strong forcing (Figs. 10b–d) and the afternoon maximum under weak forcing (Figs. 10f–h)] of IC_SMALL are similar to those of IC_MULTI. This suggests that the magnitude of the forecast error is mainly dominated by large-scale flow but moist convection determines the trend (Nielsen and Schumacher, 2016).

Regarding precipitation uncertainties, initial small-scale errors produce R within the meso-γ-scale and gradually extend to larger scales (Figs. 12c and d). Specifically, in the strong-forcing regime, the distribution peak of R does not shift to a meso-β-scale within 2–4 h (Fig. 12c) compared with IC_MULTI (Fig. 12a) and is followed by a clear decay after 4 h. Inconsistent with the strong-forcing regime, R exhibits a slight increase between 2 and 8 h (blue to yellow curves in Fig. 12d) and remains large afterward as a result of consistent up-amplitude growth of small-scale NRMDTE (Fig. 10f) in the weak-forcing regime. In summary, initial small-scale errors can gradually grow up-amplitude and upscale, causing a dispersion within ensemble members during the weak-forcing regime, reflecting greater sensitivity than in the strong-forcing regime (Weyn and Durran, 2019).

4.3. *Role of larger-scale initial errors*

Flow-dependent larger-scale initial errors generally correspond to uncertainties of the larger-scale systems (e.g., mei-yu front). The total NRMDTE in IC_LARGE shows similar temporal (Figs. 10a and e) and spatial (Figs. 14a and e) features with IC_MULTI (Figs. 10a, e and Figs. 11a, e) after 4 h. A further comparison of NRMDTEs between IC_LARGE and IC_MULTI at different scales reveals that, even in the absence of small-scale errors in the initial state, the small-scale component is still rapidly generated (Figs. 10b and f; Figs. 14b and f) and then transferred to the larger scale (Figs. 10d and h; Figs. 14d and h), corresponding to the downscale cascade as proposed by Durran and Gingrich (2014). Additionally, we can also see the total NRMDTE in IC_LARGE is obviously larger than that of IC_SMALL for both regimes (Figs. 10a and e). These results highlight that larger-scale initial errors generally control the error growth after 4 h while the errors at smaller scales are only effective at early lead times.

Figures 12 e–h display the precipitation uncertainties in IC_LARGE. At 0.5 h, R in IC_LARGE is lower than that in IC_SMALL, revealing that larger-scale initial errors do not immediately impact the precipitation. At later times, R in IC_LARGE (Figs. 12e and f) is found to be similar to that of IC_MULTI (Figs. 12a and b) for both subsets, indicating that the limit of practical predictability of precipitation can be extended by reducing the initial errors at the larger scale

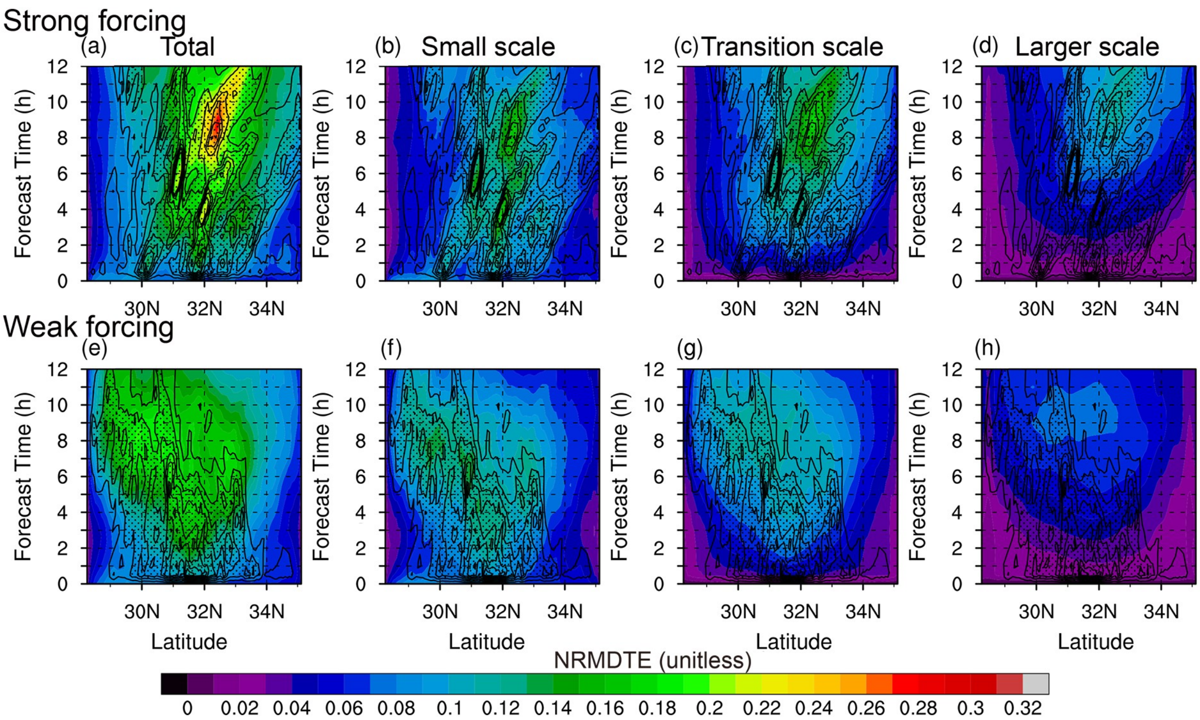

Fig. 13. As in Fig. 11 but for IC_SMALL.

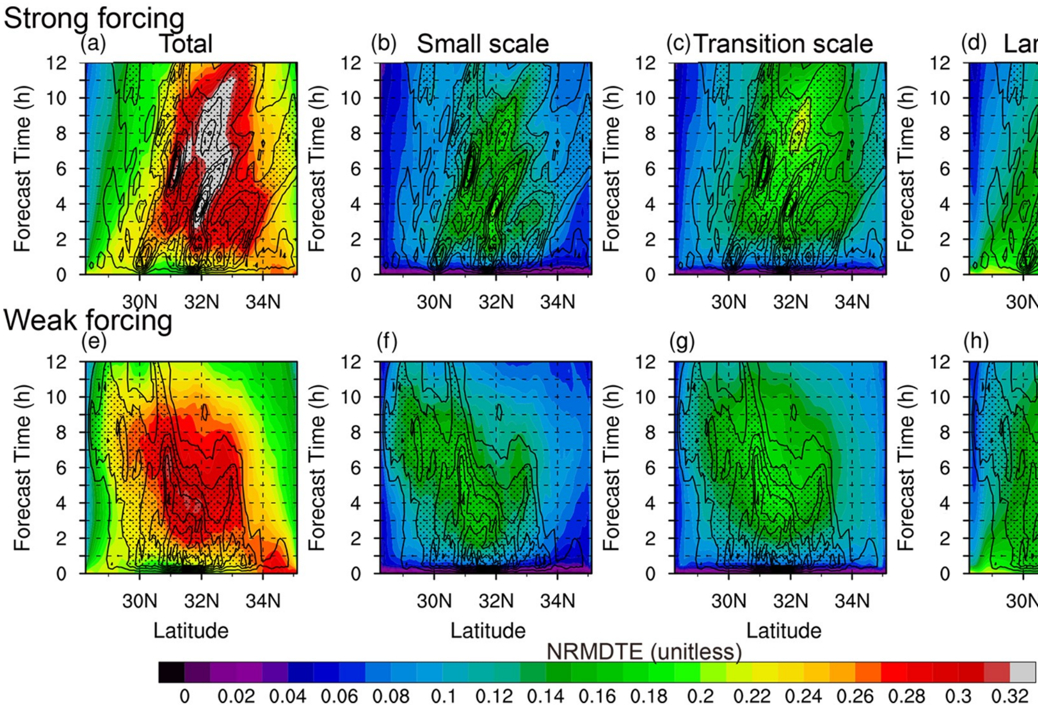

Fig. 14. As in Fig. 11 but for IC_LARGE.

and emphasizing the necessity and importance of larger-scale perturbations in ensemble design (Johnson and Wang, 2016; Surcel et al., 2016). Specifically, R in the strong-forcing regime displays a clear change in distribution during 2–4 h (blue and cyan curves in Fig. 12e) at scales < 40 km and decays afterward. By contrast, R keeps a consistent increase during the entire forecast range with a monotonical distribution in the weak-forcing regime, which relates to the local instability under unstable environments (i.e., higher CAPE) that stabilizes the spatial error propagation and destroys mesoscale predictability eventually.

Additionally, the scale-based experiments shown in Fig. 10 can also be regarded as "reduced" experiments (Nielsen and Schumacher, 2016; Zhang et al., 2016; Flora et al., 2018) that can be used to detect practical versus intrinsic predictability by examining whether the ratio for NRMDTE evolution of a "reduced" ensemble over IC_MULTI remains constant or rapidly converges to one. In this study covering the YHRB, a converging tendency within ensemble experiments in both strong- and weak-forcing regimes is found (Fig. 10) at the small and transition scales, suggesting intrinsic predictability limits at relevant scales even within a 12-h forecast range. This result corroborates the conclusion by Nielsen and Schumacher (2016) that the magnitude of error growth is governed by the interaction of moist convection with the large-scale flow.

5. Conclusions

Throughout the last three decades, the mechanisms of warm-season convective events over the YHRB have been well understood (Ding, 1993; Sun and Zhang, 2012; Luo et al., 2013, 2014; Zheng et al., 2016), whereas relevant studies on predictability, especially on the small scales, which is key to the convective-scale numerical forecast, remain scarce. In the present study, the forecast error growth (ensemble variability) and associated impact on precipitation (precipitation uncertainties) within convective-scale ensemble forecasts have been systematically investigated through 13 cases to better understand the predictability of convective events dominated by different large-scale forcings over the YHRB. In particular, this study considers: (1) whether the growth of flow-dependent initial error and associated impact on precipitation are dependent on different convective regimes; and (2) the sensitivity of LBC errors and realistic flow-dependent IC errors at different scales.

We designed an OSSE-based ensemble data assimilation and forecast system to produce realistic flow-dependent IC/LBC perturbations and initialize convective-scale ensemble forecast within a 12 h forecast range (CTRL), applied the convective adjustment timescale (Done et al., 2006) to differentiate convective regimes controlled by different large-scale forcings, compared spatiotemporal error growth based on NRMDTE at different scales across convective regimes, and applied the power ratio (R) of the decorrelation scale to measure the precipitation uncertainty in terms of spatial scale. The sensitivities of LBC and IC errors at different scales were further assessed using several scale-based ensemble sensitivity experiments (IC_MULTI, IC_SMALL, IC_TRANS, and IC_LARGE).

The investigation of CTRL revealed that the error growth dynamics are highly regime-dependent, leading to varying precipitation uncertainties within the 12-h forecast range. In general, the weak-forcing events (characterized by weaker large-scale advection and higher CAPE) are less predictable, a conclusion consistent with those of previous work (Done et al., 2012; Keil et al., 2014; Klasa et al., 2019). Specifically, the forecast error under strong forcing exhibits a stepwise feature similar to that seen in Zhang et al. (2007), while the error growth under weak forcing exhibits larger variability with a peak that corresponds to the solar-forced daytime peak phase for mei-yu-season convection over the YHRB (Sun and Zhang, 2012). The corresponding assessment of precipitation uncertainties shows a strong relationship between precipitation and error growth: the up-amplitude growth of NRMDTE determines the magnitude of R at a given scale, while the upscale growth of NRMDTE before saturation influences the distribution of R across scales during the same period.

A comparison of CTRL and IC_MULTI reveals that LBC errors impose a quasi-linear increase in the magnitude of NRMDTE in both regimes, indicating that the magnitude of the forecast error is primarily driven by the large-scale flow. Specifically, in the absence of LBC errors, the associated R under strong forcing shows a consistent decay within 4 h, revealing the importance of LBC perturbation in the ensemble design, especially for the strongly forced mei-yu frontal events.

The evaluations of IC_SMALL and IC_LARGE demonstrate that scale interaction, including upscale transfer of small-scale errors and downscale cascade of larger-scale errors, is evident in both convective regimes. Generally, small-scale IC errors are effective during the first 4 h and cause precipitation uncertainties at the meso-γ-scale, while the larger-scale IC errors are responsible for the magnitude of forecast error during the subsequent forecast range and produce precipitation uncertainties at the meso-β-scale. This result indicates that the limit of practical predictability can apparently be extended by reducing the initial errors at larger-scale (Sun and Zhang, 2016) and highlights the relative importance of initial perturbations at larger scales in ensemble design (Johnson et al., 2014; Surcel et al., 2017). Thus, the scale-blending method (Caron, 2013; Wang et al., 2014) can be employed in convective-scale ensemble forecast systems to introduce larger-scale perturbations produced by a coarser resolution ensemble forecast system that better sample the uncertainties of synoptic weather systems. We also find that small-scale IC errors are more sensitive in the weak-forcing regime than that in the strong-forcing regime. To improve the ensemble design, the model resolution can be enhanced to allow more error growth at small scales when local instability plays more important roles.

This study focuses on the practical predictability within convective-scale ensemble forecasts of warm-season convective events in the YHRB. The influence of intrinsic predictability is also determined as all the forecast errors for all the scale-based sensitivity experiments exhibit convergence tendency. These findings provide insights into convective-scale predictability, particularly the regime-dependent features, which has not been demonstrated previously. However, our final goal is to build an operational convective-scale ensemble forecast applicable to the YHRB, a task for which the domain size used in this study may not be sufficiently large. A discussion on the optimal configuration for building a convective-scale ensemble forecast remains the subject of future consideration.

Acknowledgements. The authors would also like to thank Samuel J. CHILDS from Colorado State University for language editing. This work was supported by the National Key Research and Development Program of China (Grant No. 2017YFC1502103), the National Natural Science Foundation of China (Grant Nos. 41430427 and 41705035), the China Scholarship Council, and the Postgraduate Research & Practice Innovation Program of Jiangsu Province (Grant No. KYCX17_0876).

APPENDIX A

DESCRIPTION OF ERROR

We used the difference total energy (DTE) to represent energy differences between ensemble members. A vertical function (Nielsen and Schumacher, 2016) is introduced to calculate the vertically integrated root-mean DTE (RMDTE):

$$\mathrm{RMDTE}(\lambda)_{i,j,t} = \sqrt{\frac{1}{n_{\mathrm{members}}}\sum_{m=1}^{n_{\mathrm{members}}}\sum_{k=1}^{n_{\mathrm{levels}}}\frac{p(k+1)-p(k)}{p(0)}\frac{1}{2}\left[u(\lambda)'^{2}_{i,j,k,t,m}+v(\lambda)'^{2}_{i,j,k,t,m}+\frac{C_p}{T_r}t(\lambda)'^{2}_{i,j,k,t,m}\right]}, \quad \text{(A1)}$$

where n_{members} is the number of ensemble members, the subscripts i, j, k, t, and m represent the x-direction, y-direction, vertical level, forecast time, and ensemble member, respectively. λ is the spatial scale. As vertical sub-tropospheric layers are typically used to model convective weather, n_{levels} represents vertical layers from 1000 to 100 hPa, with p denoting the pressure at each vertical layer. The three-dimensional error field for the inner domain was created using Eq. (A1).

As RMDTE values can vary by convective event, we used a method proposed in Nielsen and Schumacher (2016) to compare different cases by calculating their associated normalized RMDTEs (NRMDTEs) as the ratio of RMDTE to total mean kinetic energy (TMKE). The TMKE and its integrated form for a specific region are given as

$$\mathrm{iDTE}(\lambda)_{i,j,t} = \frac{1}{n_{\mathrm{members}}}\sum_{m=1}^{n_{\mathrm{members}}}\sum_{k=1}^{n_{\mathrm{levels}}}\frac{p(k+1)-p(k)}{p(0)}\times \frac{1}{2}\left[u(\lambda)'^{2}_{i,j,k,t,m}+v(\lambda)'^{2}_{i,j,k,t,m}+\frac{C_p}{T_r}t(\lambda)'^{2}_{i,j,k,t,m}\right]$$

$$\mathrm{TMKE}(\lambda)_{i,j,k,t} = \frac{1}{n_{\mathrm{members}}}\sum_{m=1}^{n_{\mathrm{members}}}\frac{1}{2}\left[u(\lambda)^{2}_{i,j,k,t,m}+v(\lambda)^{2}_{i,j,k,t,m}\right], \quad \text{(A2)}$$

$$\mathrm{iTMKE}(\lambda)_{i,j,t} = \sum_{k=0}^{n_{\mathrm{levels}}} \frac{p(k+1)-p(k)}{p(0)} \left(\mathrm{TMKE}(\lambda)_{i,j,k,t}\right) . \tag{A3}$$

The temperature term is excluded from Eq. (A3) to allow the TMKE to vary with the convective situation in question. Thus, the NRMDTE can be calculated as

$$\mathrm{NRMDTE}(\lambda)_{i,j,t} = \sqrt{\frac{\mathrm{iDTE}(\lambda)_{i,j,t}}{\mathrm{iTMKE}(\lambda)_{i,j,t}}} . \tag{A4}$$

The growth of errors at different scales can be assessed by computing NRMDTE over time, which, according to Lorenz (1969), can also be used to represent predictability: as the region-averaged NRMDTE gradually increases, predictability decreases.

APPENDIX B

CONVECTIVE ADJUSTMENT TIMESCALE

The convective adjustment timescale is defined as the rate at which CAPE is removed by diabatic heating associated with precipitation (Done et al., 2006):

$$\tau_{\mathrm{c}} = \frac{1}{2} \frac{C_p \rho_0 T_0}{L_{\mathrm{v}} g} \frac{\mathrm{CAPE}}{p_{\mathrm{rate}}} , \tag{B1}$$

where C_p is the specific heat capacity of air at constant pressure, ρ_0 and T_0 are the reference density and temperature, L_{v} is the latent heat of vaporization, g is the acceleration of gravity, and p_{rate} is the precipitation rate. In this study, the deterministic forecast for the inner domain is used to calculate τ_{c}. Prior to calculation, the CAPE and p_{rate} are both spatially smoothed using a Gaussian method (Keil et al., 2014) with a spatial scale of 36 km and masked with a threshold of 0.5 mm h^{-1} to avoid dry events (Surcel et al., 2016).

REFERENCES

Anderson, J. L., and S. L. Anderson, 1999: A monte carlo implementation of the nonlinear filtering problem to produce ensemble assimilations and forecasts. *Mon. Wea. Rev.*, **127**, 2741–2758, https://doi.org/10.1175/1520-0493(1999)127<2741:AMCIOT>2.0.CO;2.

Bachmann, K., C. Keil, and M. Weissmann, 2019: Impact of radar data assimilation and orography on predictability of deep convection. *Quart. J. Roy. Meteorol. Soc.*, **145**, 117–130, https://doi.org/10.1002/qj.3412.

Bachmann, K., C. Keil, G. C. Craig, M. Weissmann, and C. A. Welzbacher, 2020: Predictability of deep convection in idealized and operational forecasts: Effects of radar data assimilation, orography, and synoptic weather regime. *Mon. Wea. Rev.*, **148**, 63–81, https://doi.org/10.1175/MWR-D-19-0045.1.

Bei, N. F., and F. Q. Zhang, 2007: Impacts of initial condition errors on mesoscale predictability of heavy precipitation along the Mei-Yu front of China. *Quart. J. Roy. Meteorol. Soc.*, **133**, 83–99, https://doi.org/10.1002/qj.20.

Bei, N. F., and F. Q. Zhang, 2014: Mesoscale predictability of moist baroclinic waves: Variable and scale-dependent error growth. *Adv. Atmos. Sci.*, **31**, 995–1008, https://doi.org/10.1007/s00376-014-3191-7.

Bierdel, L., T. Selz, and G. C. Craig, 2017: Theoretical aspects of upscale error growth through the mesoscales: An analytical model. *Quart. J. Roy. Meteorol. Soc.*, **143**, 3048–3059, https://doi.org/10.1002/qj.3160.

Caron, J.-F., 2013: Mismatching perturbations at the lateral boundaries in limited-area ensemble forecasting: A case study. *Mon. Wea. Rev.*, **141**, 356–374, https://doi.org/10.1175/MWR-D-12-00051.1.

Chen, X., H. L. Yuan, and M. Xue, 2018: Spatial spread-skill relationship in terms of agreement scales for precipitation forecasts in a convection-allowing ensemble. *Quart. J. Roy. Meteorol. Soc.*, **144**, 85–98, https://doi.org/10.1002/qj.3186.

Chen, Y., Y. Chen, T. Chen, and H. He, 2016: Characteristics analysis of warm sector rainstorms over the middle lower reaches of the Yangtze River. *Meteorol. Mon.*, **42**, 724–731, https://doi.org/10.7519/j.issn.1000-0526.2016.06.008. (in Chinese with English abstract)

Chou, M. D., and M. J. Suarez, 1999: A solar radiation parameterization (CLIRAD-SW) for atmospheric studies. *NASA Tech. Memo*, 10460.

Daniels, M. H., K. A. Lundquist, J. D. Mirocha, D. J. Wiersema, and F. K. Chow, 2016: A new vertical grid nesting capability in the Weather Research and Forecasting (WRF) model. *Mon. Wea. Rev.*, **144**, 3725–3747, https://doi.org/10.1175/MWR-D-16-0049.1.

Denis, B., J. Côté, and R. Laprise, 2002: Spectral decomposition of two-dimensional atmospheric fields on limited-area domains using the Discrete Cosine Transform (DCT). *Mon. Wea. Rev.*, **130**, 1812–1829, https://doi.org/10.1175/1520-0493(2002)130<1812:SDOTDA>2.0.CO;2.

Ding, Y. H., 1993: *Study on the Lasting Heavy Rainfalls over the Yangtze-Huaihe River Basin in 1991*. China Meteorological Press. (in Chinese)

Done, J. M., G. C. Craig, S. L. Gray, P. A. Clark, and M. E. B. Gray, 2006: Mesoscale simulations of organized convection: Importance of convective equilibrium. *Quart. J. Roy. Meteorol. Soc.*, **132**, 737–756, https://doi.org/10.1256/qj.04.84.

Done, J. M., G. C. Craig, S. L. Gray, and P. A. Clark, 2012: Case-to-case variability of predictability of deep convection in a mesoscale model. *Quart. J. Roy. Meteorol. Soc.*, **138**, 638–648, https://doi.org/10.1002/qj.943.

Durran, D. R., and M. Gingrich, 2014: Atmospheric predictability: Why butterflies are not of practical importance. *J. Atmos. Sci.*, **71**, 2476–2488, https://doi.org/10.1175/JAS-D-14-0007.1.

Durran, D. R., and J. A. Weyn, 2016: Thunderstorms do not get butterflies. *Bull. Amer. Meteorol. Soc.*, **97**, 237–243, https://doi.org/10.1175/BAMS-D-15-00070.1.

Flack, D. L. A., R. S. Plant, S. L. Gray, H. W. Lean, C. Keil, and G. C. Craig, 2016: Characterisation of convective regimes over the British Isles. *Quart. J. Roy. Meteorol. Soc.*, **142**, 1541–1553, https://doi.org/10.1002/qj.2758.

Flack, D. L. A., S. L. Gray, R. S. Plant, H. W. Lean, and G. C. Craig, 2018: Convective-scale perturbation growth across the spectrum of convective regimes. *Mon. Wea. Rev.*, **146**, 387–405, https://doi.org/10.1175/MWR-D-17-0024.1.

Flora, M. L., C. K. Potvin, and L. J. Wicker, 2018: Practical predictability of supercells: Exploring ensemble forecast sensitivity to initial condition spread. *Mon. Wea. Rev.*, **146**, 2361–2379, https://doi.org/10.1175/MWR-D-17-0374.1.

Fu, S. M., F. Yu, D. H. Wang, and R. D. Xia, 2013: A comparison of two kinds of eastward-moving mesoscale vortices during the mei-yu period of 2010. *Science China Earth Sciences*, **56**, 282–300, https://doi.org/10.1007/s11430-012-4420-5.

Gasperoni, N. A., M. Xue, R. D. Palmer, and J. D. Gao, 2013: Sensitivity of convective initiation prediction to near-surface moisture when assimilating radar refractivity: Impact tests using OSSEs. *J. Atmos. Oceanic Technol.*, **30**, 2281–2302, https://doi.org/10.1175/JTECH-D-12-00038.1.

Grell, G. A., and D. Dévényi, 2002: A generalized approach to parameterizing convection combining ensemble and data assimilation techniques. *Geophys. Res. Lett.*, **29**, 1693, https://doi.org/10.1029/2002GL015311.

Hagedorn, R., T. M. Hamill, and J. S. Whitaker, 2008: Probabilistic forecast calibration using ECMWF and GFS ensemble reforecasts. Part I: Two-meter temperatures. *Mon. Wea. Rev.*, **136**, 2608–2619, https://doi.org/10.1175/2007MWR2410.1.

Hagedorn, R., R. Buizza, T. M. Hamill, M. Leutbecher, and T. N. Palmer, 2012: Comparing TIGGE multimodel forecasts with reforecast-calibrated ECMWF ensemble forecasts. *Quart. J. Roy. Meteorol. Soc.*, **138**, 1814–1827, https://doi.org/10.1002/qj.1895.

Hohenegger, C., and C. Schär, 2007: Predictability and error growth dynamics in cloud-resolving models. *J. Atmos. Sci.*, **64**, 4467–4478, https://doi.org/10.1175/2007JAS2143.1.

Hohenegger, C., D. Lüthi, and C. Schär, 2006: Predictability mysteries in cloud-resolving models. *Mon. Wea. Rev.*, **134**, 2095–2107, https://doi.org/10.1175/MWR3176.1.

Hong, S.-Y., and J.-O. J. Lim, 2006: The WRF single-moment 6-class microphysics scheme (WSM6). *Journal of the Korean Meteorological Society*, **42**, 129–151.

Hong, S.-Y., Y. Noh, and J. Dudhia, 2006: A new vertical diffusion package with an explicit treatment of entrainment processes. *Mon. Wea. Rev.*, **134**, 2318–2341, https://doi.org/10.1175/MWR3199.1.

Johnson, A., and Coauthors, 2014: Multiscale characteristics and evolution of perturbations for warm season convection-allowing precipitation forecasts: Dependence on background flow and method of perturbation. *Mon. Wea. Rev.*, **142**, 1053–1073, https://doi.org/10.1175/MWR-D-13-00204.1.

Johnson, A., and X. G. Wang, 2016: A study of multiscale initial condition perturbation methods for convection-permitting ensemble forecasts. *Mon. Wea. Rev.*, **144**, 2579–2604, https://doi.org/10.1175/MWR-D-16-0056.1.

Johnson, A., X. G. Wang, J. R. Carley, L. J. Wicker, and C. Karstens, 2015: A comparison of multiscale GSI-based EnKF and 3DVar data assimilation using radar and conventional observations for midlatitude convective-scale precipitation forecasts. *Mon. Wea. Rev.*, **143**, 3087–3108, https://doi.org/10.1175/MWR-D-14-00345.1.

Judt, F., 2018: Insights into atmospheric predictability through global convection-permitting model simulations. *J. Atmos. Sci.*, **75**, 1477–1497, https://doi.org/10.1175/JAS-D-17-0343.1.

Keil, C., and G. C. Craig, 2011: Regime-dependent forecast uncertainty of convective precipitation. *Meteorol. Z.*, **20**, 145–151, https://doi.org/10.1127/0941-2948/2011/0219.

Keil, C., F. Heinlein, and G. C. Craig, 2014: The convective adjustment time-scale as indicator of predictability of convective precipitation. *Quart. J. Roy. Meteorol. Soc.*, **140**, 480–490, https://doi.org/10.1002/qj.2143.

Keil, C., F. Baur, K. Bachmann, S. Rasp, L. Schneider, and C. Barthlott, 2019: Relative contribution of soil moisture, boundary-layer and microphysical perturbations on convective predictability in different weather regimes. *Quart. J. Roy. Meteorol. Soc.*, **145**, 3102–3115, https://doi.org/10.1002/qj.3607.

Klasa, C., M. Arpagaus, A. Walser, and H. Wernli, 2019: On the time evolution of limited-area ensemble variance: Case studies with the convection-permitting ensemble COSMO-E. *J. Atmos. Sci.*, **76**, 11–26, https://doi.org/10.1175/JAS-D-18-0013.1.

Kühnlein, C., C. Keil, G. C. Craig, and C. Gebhardt, 2014: The impact of downscaled initial condition perturbations on convective-scale ensemble forecasts of precipitation. *Quart. J. Roy. Meteorol. Soc.*, **140**, 1552–1562, https://doi.org/10.1002/qj.2238.

Lean, H. W., P. A. Clark, M. Dixon, N. M. Roberts, A. Fitch, R. Forbes, and C. Halliwell, 2008: Characteristics of high-resolution versions of the met office unified model for forecasting convection over the United Kingdom. *Mon. Wea. Rev.*, **136**, 3408–3424, https://doi.org/10.1175/2008MWR2332.1.

Liu, J. Y., and Z.-M. Tan, 2009: Mesoscale predictability of mei-yu heavy rainfall. *Adv. Atmos. Sci.*, **26**, 438–450, https://doi.org/10.1007/s00376-009-0438-9.

Liu, J. Y., Z. M. Tan, and Y. Zhang, 2012: Study of the three types of torrential rains of different formation mechanism during the Meiyu period. *Acta Meteorologica Sinica*, **70**, 452–466, https://doi.org/10.11676/qxxb2012.038.

Lorenz, E. N., 1969: Atmospheric predictability as revealed by naturally occurring analogues. *J. Atmos. Sci.*, **26**, 636–646, https://doi.org/10.1175/1520-0469(1969)26<636:APARBN>2.0.CO;2.

Luo, Y. L., and Y. R. X. Chen, 2015: Investigation of the predictability and physical mechanisms of an extreme-rainfall-producing mesoscale convective system along the Meiyu front in East China: An ensemble approach. *J. Geophys. Res.: Atmos.*, **120**, 10593–10618, https://doi.org/10.1002/2015JD023584.

Luo, Y. L., Y. Gong, and D.-L. Zhang, 2014: Initiation and organizational modes of an extreme-rain-producing mesoscale convective system along a Mei-Yu Front in East China. *Mon. Wea. Rev.*, **142**, 203–221, https://doi.org/10.1175/MWR-D-13-00111.1.

Luo, Y. L., W. M. Qian, R. H. Zhang, and D.-L. Zhang, 2013: Gridded hourly precipitation analysis from high-density rain gauge network over the Yangtze-Huai Rivers Basin during the 2007 Mei-Yu season and comparison with CMORPH. *Journal of Hydrometeorology*, **14**, 1243–1258, https://doi.org/10.1175/JHM-D-12-0133.1.

Madaus, L. E., and G. J. Hakim, 2017: Constraining ensemble forecasts of discrete convective initiation with surface observations. *Mon. Wea. Rev.*, **145**, 2597–2610, https://doi.org/10.1175/MWR-D-16-0395.1.

Mass, C. F., D. Ovens, K. Westrick, and B. A. Colle, 2002: Does increasing horizontal resolution produce more skillful forecasts? The results of two years of real-time numerical weather prediction over the Pacific Northwest *Bull. Amer. Meteorol. Soc.*, **83**, 407–430, https://doi.org/10.1175/1520-0477(2002)083<0407:DIHRPM>2.3.CO;2.

Melhauser, C., and F. Q. Zhang, 2012: Practical and intrinsic predictability of severe and convective weather at the mesoscales. *J. Atmos. Sci.*, **69**, 3350–3371, https://doi.org/10.1175/JAS-D-11-0315.1.

Mlawer, E. J., S. J. Taubman, P. D. Brown, M. J. Iacono, and S. A. Clough, 1997: Radiative transfer for inhomogeneous atmospheres: RRTM, a validated correlated-k model for the longwave. *J. Geophys. Res.: Atmos.*, **102**, 16663–16682, https://doi.org/10.1029/97JD00237.

Nielsen, E. R., and R. S. Schumacher, 2016: Using convection-allowing ensembles to understand the predictability of an extreme rainfall event. *Mon. Wea. Rev.*, **144**, 3651–3676, https://doi.org/10.1175/MWR-D-16-0083.1.

Nutter, P., D. Stensrud, and M. Xue, 2004: Effects of coarsely resolved and temporally interpolated lateral boundary conditions on the dispersion of limited-area ensemble forecasts. *Mon. Wea. Rev.*, **132**, 2358–2377, https://doi.org/10.1175/1520-0493(2004)132<2358:EOCRAT>2.0.CO;2.

Raynaud, L., and F. Bouttier, 2016: Comparison of initial perturbation methods for ensemble prediction at convective scale. *Quart. J. Roy. Meteorol. Soc.*, **142**, 854–866, https://doi.org/10.1002/qj.2686.

Selz, T., and G. C. Craig, 2015: Upscale error growth in a high-resolution simulation of a summertime weather event over Europe. *Mon. Wea. Rev.*, **143**, 813–827, https://doi.org/10.1175/MWR-D-14-00140.1.

Selz, T., L. Bierdel, and G. C. Craig, 2019: Estimation of the variability of mesoscale energy spectra with three years of COSMO-DE analyses. *J. Atmos. Sci.*, **76**, 627–637, https://doi.org/10.1175/JAS-D-18-0155.1.

Skamarock, W. C., and Coauthors, 2008: A description of the Advanced Research WRF version 3. NCAR Tech. Note-475+ STR.

Snook, N., M. Xue, and Y. Jung, 2015: Multiscale EnKF assimilation of radar and conventional observations and ensemble forecasting for a tornadic mesoscale convective system. *Mon. Wea. Rev.*, **143**, 1035–1057, https://doi.org/10.1175/MWR-D-13-00262.1.

Sun, J. H., and F. Q. Zhang, 2012: Impacts of mountain-plains solenoid on diurnal variations of rainfalls along the Mei-Yu front over the East China plains. *Mon. Wea. Rev.*, **140**, 379–397, https://doi.org/10.1175/MWR-D-11-00041.1.

Sun, Y. Q., and F. Q. Zhang, 2016: Intrinsic versus Practical limits of atmospheric predictability and the significance of the butterfly effect. *J. Atmos. Sci.*, **73**, 1419–1438, https://doi.org/10.1175/JAS-D-15-0142.1.

Surcel, M., I. Zawadzki, and M. K. Yau, 2015: A study on the scale dependence of the predictability of precipitation patterns. *J. Atmos. Sci.*, **72**, 216–235, https://doi.org/10.1175/JAS-D-14-0071.1.

Surcel, M., I. Zawadzki, and M. K. Yau, 2016: The case-to-case variability of the predictability of precipitation by a storm-scale ensemble forecasting system. *Mon. Wea. Rev.*, **144**, 193–212, https://doi.org/10.1175/MWR-D-15-0232.1.

Surcel, M., I. Zawadzki, M. K. Yau, M. Xue, and F. Y. Kong, 2017: More on the scale dependence of the predictability of precipitation patterns: Extension to the 2009-13 CAPS spring experiment ensemble forecasts. *Mon. Wea. Rev.*, **145**, 3625–3646, https://doi.org/10.1175/MWR-D-16-0362.1.

Tan, Z.-M., F. Q. Zhang, R. Rotunno, and C. Snyder, 2004: Mesoscale predictability of moist baroclinic waves: Experiments with parameterized convection. *J. Atmos. Sci.*, **61**, 1794–1804, https://doi.org/10.1175/1520-0469(2004)061<1794:MPOMBW>2.0.CO;2.

Tennant, W., 2015: Improving initial condition perturbations for MOGREPS-UK. *Quart. J. Roy. Meteorol. Soc.*, **141**, 2324–2336, https://doi.org/10.1002/qj.2524.

Tong, M. J., and M. Xue, 2005: Ensemble Kalman filter assimilation of doppler radar data with a compressible nonhydrostatic model: OSS experiments. *Mon. Wea. Rev.*, **133**, 1789–1807, https://doi.org/10.1175/MWR2898.1.

Toth, Z., and E. Kalnay, 1997: Ensemble forecasting at NCEP and the breeding method. *Mon. Wea. Rev.*, **125**, 3297–3319, https://doi.org/10.1175/1520-0493(1997)125<3297:EFANAT>2.0.CO;2.

Vié, B., O. Nuissier, and V. Ducrocq, 2011: Cloud-resolving ensemble simulations of mediterranean heavy precipitating events: Uncertainty on initial conditions and lateral boundary conditions. *Mon. Wea. Rev.*, **139**, 403–423, https://doi.org/10.1175/2010MWR3487.1.

Walser, A., D. Lüthi, and C. Schär, 2004: Predictability of precipitation in a cloud-resolving model. *Mon. Wea. Rev.*, **132**, 560–577, https://doi.org/10.1175/1520-0493(2004)132<0560:POPIAC>2.0.CO;2.

Wang, S. Z., M. Xue, A. D. Schenkman, and J. Z. Min, 2013: An iterative ensemble square root filter and tests with simulated radar data for storm-scale data assimilation. *Quart. J. Roy. Meteorol. Soc.*, **139**, 1888–1903, https://doi.org/10.1002/qj.2077.

Wang, Y., M. Bellus, J.-F. Geleyn, X. L. Ma, W. H. Tian, and F. Weidle, 2014: A new method for generating initial condition perturbations in a regional ensemble prediction system: Blending. *Mon. Wea. Rev.*, **142**, 2043–2059, https://doi.org/10.1175/MWR-D-12-00354.1.

Weyn, J. A., and D. R. Durran, 2017: The dependence of the predictability of mesoscale convective systems on the horizontal scale and amplitude of initial errors in idealized simulations. *J. Atmos. Sci.*, **74**, 2191–2210, https://doi.org/10.1175/JAS-D-17-0006.1.

Weyn, J. A., and D. R. Durran, 2019: The scale dependence of initial-condition sensitivities in simulations of convective systems over the southeastern United States. *Quart. J. Roy. Meteorol. Soc.*, **145**, 57–74, https://doi.org/10.1002/qj.3367.

Whitaker, J. S., and T. M. Hamill, 2002: Ensemble Data Assimilation without Perturbed Observations. *Mon. Wea. Rev.*, **130**, 1913–1924, https://doi.org/10.1175/1520-0493(2002)130<1913:EDAWPO>2.0.CO;2.

Wu, N. G., X. R. Zhuang, J. Z. Min, and Z. Y. Meng, 2020: Practical and intrinsic predictability of a warm-sector torrential rainfall event in the South China monsoon region. *J. Geophys. Res.: Atmos.*, **125**, e2019JD031313, https://doi.org/10.1029/2019JD031313.

Yussouf, N., and D. J. Stensrud, 2012: Comparison of single-parameter and multiparameter ensembles for assimilation of radar observations using the ensemble kalman filter. *Mon. Wea. Rev.*, **140**, 562–586, https://doi.org/10.1175/MWR-D-10-05074.1.

Zhang, F., C. Snyder, and R. Rotunno, 2003: Effects of moist convection on mesoscale predictability. *J. Atmos. Sci.*, **60**, 1173–1185, https://doi.org/10.1175/1520-0469(2003)060<1173:EOMCOM>2.0.CO;2.

Zhang, F., C. Snyder, and J. Z. Sun, 2004: Impacts of initial estimate and observation availability on convective-scale data assimilation with an ensemble Kalman filter. *Mon. Wea. Rev.*, **132**, 1238–1253, https://doi.org/10.1175/1520-0493

(2004)132<1238:IOIEAO>2.0.CO;2.

Zhang, F. Q., A. M. Odins, and J. W. Nielsen-Gammon, 2006: Mesoscale predictability of an extreme warm-season precipitation event. *Wea. Forecasting*, **21**, 149–166, https://doi.org/10.1175/WAF909.1.

Zhang, F. Q., N. F. Bei, R. Rotunno, C. Snyder, and C. C. Epifanio, 2007: Mesoscale predictability of moist baroclinic waves: Convection-permitting experiments and multistage error growth dynamics. *J. Atmos. Sci.*, **64**, 3579–3594, https://doi.org/10.1175/JAS4028.1.

Zhang, L., J. Z. Min, X. R. Zhuang, and R. S. Schumacher, 2019: General features of extreme rainfall events produced by MCSs over East China during 2016-17. *Mon. Wea. Rev.*, **147**, 2693–2714, https://doi.org/10.1175/MWR-D-18-0455.1.

Zhang, M., and D.-L. Zhang, 2012: Subkilometer simulation of a torrential-rain-producing mesoscale convective system in East China. Part I: Model verification and convective organization. *Mon. Wea. Rev.*, **140**, 184–201, https://doi.org/10.1175/MWR-D-11-00029.1.

Zhang, X. B., 2019: Multiscale characteristics of different-source perturbations and their interactions for convection-permitting ensemble forecasting during SCMREX. *Mon. Wea. Rev.*, **147**, 291–310, https://doi.org/10.1175/MWR-D-18-0218.1.

Zhang, Y. J., F. Q. Zhang, D. J. Stensrud, and Z. Y. Meng, 2016: Intrinsic predictability of the 20 May 2013 Tornadic thunderstorm event in Oklahoma at Storm Scales. *Mon. Wea. Rev.*, **144**, 1273–1298, https://doi.org/10.1175/MWR-D-15-0105.1.

Zhao, S. X., L. S. Zhang, and J. H. Sun, 2007: Study of heavy rainfall and related mesoscale systems causing severe flood in Huaihe River basin during the summer of 2007. *Climatic and Environmental Research*, **12**, 713–727, https://doi.org/10.3969/j.issn.1006-9585.2007.06.002. (in Chinese with English abstract)

Zheng, Y. G., M. Xue, B. Li, J. Chen, and Z. Y. Tao, 2016: Spatial characteristics of extreme rainfall over China with hourly through 24-hour accumulation periods based on national-level hourly rain gauge data. *Adv. Atmos. Sci.*, **33**, 1218–1232, https://doi.org/10.1007/s00376-016-6128-5.

Zhu, X. Y., and J. J. Zhu, 2004: New generation weather radar network in China. *Meteorological Science and Technology*, **32**, 255–258, https://doi.org/10.3969/j.issn.1671-6345.2004.04.012. (in Chinese with English abstract)

Zhuang, X. R., H. N. Zhu, J. Z. Min, L. Zhang, N. G. Wu, Z. P. Wu, and S. Q. Wang, 2019: Spatial predictability of heavy rainfall events in East China and the application of spatial-based methods of probabilistic forecasting. *Atmosphere*, **10**, 490, https://doi.org/10.3390/atmos10090490.

Zhuang, X. R., N. G. Wu, J. Z. Min, and Y. Xu, 2020: Understanding the predictability within convection-allowing ensemble forecasts in East China: Meteorological sensitivity, forecast error growth and associated precipitation uncertainties across spatial scales. *Atmosphere*, **11**, 234, https://doi.org/10.3390/atmos11030234.

Zimmer, M., G. C. Craig, C. Keil, and H. Wernli, 2011: Classification of precipitation events with a convective response timescale and their forecasting characteristics. *Geophys. Res. Lett.*, **38**, L05802, https://doi.org/10.1029/2010GL046199.